UNIVERSITAT POLITÈCNICA DE CATALUNYA BARCELONATECH

Design and implementation of an SDR-based multi-frequency ground-based SAR system

Partial disclosure document

Adrià Amézaga Sàrries

PhD. Thesis

Design and implementation of an SDR-based multi-frequency ground-based SAR system

Partial disclosure document

Author

Adrià Amézaga Sàrries

Thesis Advisors

Carlos López-Martínez

Roger Jové Casulleras

Signal Theory and Communications Department

Universitat Politècnica de Catalunya - BarcelonaTech

Barcelona, August 2020

Note about partial disclosure

This document is a partial disclosure of the full thesis. Some parts are omitted due to confidentiality agreements. References to non disclosed sections, such as figures, sections and tables, are marked with two question marks.

Abstract

Synthetic Aperture Radar (SAR) has proven a valuable tool in the monitoring of the Earth, either at a global or local scales. SAR is a coherent radar system able to image extended areas with high resolution, and finds applications in many areas such as forestry, agriculture, mining, structure inspection or security operations.

Although space-borne SAR systems can image extended areas, their main limitation is the long revisit times, which are not suitable for applications where the target experiments rapid changes, in the scale of minutes to few days. Ground-Based Synthetic Aperture Radar (GBSAR) systems have proven useful to fill this revisit time gap by imaging relatively small areas continuously, with extensions usually smaller than a few square kilometers. GBSAR systems have been used extensively for the monitoring of slope instability, and are a common tool in the mining sector.

The development of the GBSAR is relatively recent, and various developments have taken place since the 2000s, transitioning from the usage of Vector Network Analyzers (VNAs) to custom radar cores tailored for this application. This transition is accompanied by a reduction in cost, but at the same time is accompanied by a loss of operational flexibility. Specifically, most GBSAR sensors now operate at a single frequency, losing the value of the multi-band operation that VNAs provided.

This work is motivated by the idea that it is worth to use the value of multi-frequency GBSAR measurements, while maintaining a limited system cost. In order to implement a GBSAR with these characteristics, it is realized that Software Defined Radio (SDR) devices are a good option for fast and flexible implementation of broadband transceivers.

This thesis details the design and implementation process of an SDR-based Frequency Modulated Continuous Wave (FMCW) GBSAR system from the ground up, presenting the main issues related with the usage of the most common SDR analogue architecture, the Zero-IF transceiver. The main problem is determined to be the behavior of spurs related to IQ imbalances of the analogue transceiver with the FMCW demodulation process. Two effective techniques to overcome these issues, the Super Spatial Variant Apodization (SSVA) and the Short Time Fourier Transform (STFT) signal reconstruction techniques,

are implemented and tested. The thesis also deals with the digital implementation of the signal generator and digital receiver, which are implemented on top of an RF Network-on-Chip (RFNoC) architecture in the SDR Field Programmable Gate Array (FPGA). Another important aspect of this work is the development of an Radio-Frequency (RF) front-end that extends the capabilities of the SDR, implementing filtering, amplification, leakage mitigation and up-conversion to X-band. Finally, a set of test campaigns is described, in which the operation of the system is verified and the value of multi-frequency GBSAR observations is shown.

Acknowledgments

This Thesis is the result four years of work full of ups and downs. The moments of intense impetus and joy when ideas turn into reality are sometimes ended by motivation-shattering events, such as the appearance of seemingly irresolvable problems. I'm sure that everyone pursuing a PhD has experienced this, and it's the natural state of works of this kind. It is in the moments of doubt that make people around you essential. It is obvious that this work would not exist without them.

First, I would like to give an immense acknowledgment to my thesis advisor, Carlos López-Martínez. He was the main motivator for starting this work. His insights, ideas and help have been paramount into the completion of this Thesis. Also, and equally important, his humane quality and cheerfulness have been an important source of motivation. I feel very lucky to have him as my thesis director and I'm sure we will continue our collaboration.

Second, I express my gratitude to Roger Jové, the co-director of this thesis, with whom I have shared the brutal experience of starting and pushing up Balamis. He was also an essential source of motivation.

My appreciation also goes for Ricard Gonzálvez, whose technical insights have made the realization of this thesis less of a burden.

My acknowledgment also goes for Adriano Camps, my tutor. My early contact with remote sensing was due to him, who started the NanoSat Lab, where I learned things that were the foundation of what came next. His amount of motivation and capacity to push projects into reality amazes me.

I would also like to thank the Church of Sant Pere de Subirats and Ms. Ita Boada for granting access to the Subirats Castle test site.

The last acknowledgment goes for my family, for always supporting me, and Clara, who has coped with me during this time and always cheered me up when needed.

Official acknowledgments

The author thanks the support received from Spanish Ministry of Economy and Competitiveness (MINECO) and the Catalan Ministry of Business and Knowledge for its financial support to the research performed in this work under the projects DI-15-08147 and 2016 DI 012, respectively, in the frame of the industrial PhD programs.

Contents

List of Figures

List of Tables

Acronyms

ADC Analog to Digital Converter.

ALU Arithmetic-Logic Unit.

ASI Agenzia Spaziale Italiana.

ASIC Application Specific Integrated Circuit.

BRAM Block Random Access Memory.

CMOS Complementary Metal-Oxide-Semiconductor.

CW Continuous Wave.

DAC Digital to Analog Converter.

DDS Direct Digital Synthesizer.

DEM Digital Elevation Map.

DLR Deutsches Zentrum für Luft-und Raumfahrt.

DMA Direct Memory Access.

DSP Digital Signal Processor.

ESA European Space Agency.

FFT Fast Fourier Transform.

FMCW Frequency Modulated Continuous Wave.

FOV Field of View.

FPGA Field Programmable Gate Array.

GBSAR Ground-Based Synthetic Aperture Radar.

GPP General Purpose Processor.

GPR Ground Penetrating Radar.

GPU Graphical Processor Unit.

IC Integrated Circuit.

IEEE Institute of Electrical and Electronic Engineers.

IF Intermediate Frequency.

InSAR Interferometric SAR.

LFM Linear Frequency Modulation.

LNA Low Noise Amplifier.

LO Local Oscillator.

MIMO Massive Input Massive Output.

MINECO Spanish Ministry of Economy and Competitiveness.

NASA National Aeronautics and Space Administration.

OFDM Orthogonal Frequency Division Multiplex.

PA Power Amplifier.

PCB Printed Circuit Board.

PLL Phase-Locked Loop.

PolInSAR Polarimetric Interferometric SAR.

PolSAR Polarimetric SAR.

PPS pulse per second.

PRF Pulse Repetition Frequency.

PSF Point Spread Function.

RCS Radar Cross Section.

RF Radio-Frequency.

RFFE RF Front-End.

RFI Radio-Frequency Interference.

RFNoC RF Network-on-Chip.

RFSoC Radio-Frequency System-on-Chip.

RFSoM Radio-Frequency System-on-Module.

RIO Reconfigurable I/O.

ROM Read Only Memory.

RVP Residual Video Phase.

SAR Synthetic Aperture Radar.

SAW Surface Acoustic Wave.

SCR Software Controlled Radio.

SDR Software Defined Radio.

SDRadar Software Defined Radar.

SEE Single-Event Effect.

SFCW Stepped Frequency Continuous Wave.

SIMT Single Instruction, Multiple Threads.

SLAR Side Looking Airborne Radar.

SLC Single Look Complex.

SMA SubMiniature version A.

SoA State of the Art.

SoC System-on-Chip.

SRAM Static RAM.

SSVA Super Spatial Variant Apodization.

STFT Short Time Fourier Transform.

TCR Trihedral Corner Reflector.

TX transmission.

USB Universal Serial Bus.

USRP Universal Software Radio Peripheral.

UWB Ultra Wide Band.

VNA Vector Network Analyzer.

1 Introduction

1.1 SAR history and evolution

Synthetic Aperture Radar (SAR) has been used since the sixties for a plethora of applications. Its high spatial resolution, day and night imaging capability and weather-independent operation have made of it an invaluable remote sensing tool that complements other observation techniques such as optical imaging. SAR is applied in a wide range of sectors, including commercial, scientific and military, for applications ranging from small scale observations such as target detection [1] and infrastructure monitoring [2] to large-scale ones such as terrain mapping [3].

SAR was first proposed by Carl Wiley in 1951 and later patented in 1954. The concept of synthetic aperture was a breakthrough for imaging radars, that relied on the Side Looking Airborne Radar (SLAR) technique at that time [4–6]. Compared to SLAR, where azimuth resolution is inversely proportional to the antenna size, the SAR resolution is proportional to it. This fact allowed much finer azimuth resolutions for practical antenna sizes. Although the SAR technique only provides finer resolutions in azimuth, it was this finer resolution that provided an incentive to also improve range resolution [5].

The first developments of SAR were in the military field. Stemming from research and development programs aimed at improving military surveillance, SAR was regarded as a potential tool to be developed. The first systems used optical processing due to the lack of powerful digital techniques. In the 70s, digital technology advances allowed the implementation of the first digital SAR processors [5]. Since then, a constant stream of significant improvements have taken place.

The first civil space-borne SAR mission was the SEASAT mission in 1978 [7]. The SEASAT mission included an L-band SAR and its main goal was to get a better understanding of Earth's seas. Unfortunately, the mission terminated after 110 days due to a hardware failure. Nevertheless, SEASAT data demonstrated the potential of SAR

for Earth observation and spawned many subsequent Earth remote sensing missions and instruments [4].

During the 70s and the 80s, the research on SAR for civil applications became a very active field. Many airborne sensors were developed as demonstrators and were used for geophysical and biophysical parameter retrieval from the Earth surface. The advances achieved in airborne systems were then implemented in space borne systems.

Although the first SAR developments were developed in the USA, other countries were aware of the technology potential and started their own programs. ERS-1 and ERS-2 were the first space borne SAR sensors developed by the European Space Agency (ESA). Launched in 1991 and 1995, respectively, the ERS-1/2 mission was aimed at providing high quality SAR images of ocean, coastal zones, ice regions and land. The mission was a technological milestone both in instrument technology and the fact that it was the first time that two SAR satellites operated in a 'tandem' configuration. This configuration provided the opportunity to observe changes over a very short time spacing (24h between both satellite passes) [8]. In Japan, JERS-1 [9], launched in 1992, and was aimed at applications such as monitoring of geological phenomena, land use, observation of coastal regions and disaster monitoring. Canada stepped in with the RADARSAT program [10], which was commercially operated and served both scientific and commercial demands such as disaster management, interferometry, agriculture, cartography, hydrology, etc.

Throughout SAR technology development, there has been a push to increase the value of the provided data. In the 80s and 90s, new techniques such as SAR polarimetry and interferometry arose and increased the richness of available information, making new applications possible. For instance, the development of interferometry led to applications such as deformation monitoring and Digital Elevation Map (DEM) creation. On the other hand, polarimetry found applications in agriculture, oceanography, forestry and disaster monitoring [11]. Significant developments in these two fields were achieved by SIR-C/X-SAR in 1994, a joint National Aeronautics and Space Administration (NASA)/Deutsches Zentrum für Luft-und Raumfahrt (DLR)/Agenzia Spaziale Italiana (ASI) mission which consisted of L-, C- and X-band sensors mounted on the NASA Space Shuttle. Simultaneous multi frequency, fully polarized, repeat-pass interferometric capability of SIR-C/X-SAR was a major milestone in SAR development and had a profound impact on subsequent SAR missions. Differential interferometry was also developed in the 90s and the beginning of 2000s by ERS-1/2 and ENVISAT.

ENVISAT was one of the most complex European satellites. Launched in 2002 it was the first space-borne SAR sensor to implement different acquisition modes through antenna flexibility, and marked the beginning of a trend for later SAR missions. The versatility of the antenna allowed for various acquisition modes to be operated on demand. Each

acquisition mode was optimized for each application, by exploiting trade-offs in swath coverage, resolution and incidence angle.

The trends in the last years are in line with the goal of providing increased information richness. Higher spatial resolution, higher swath, reduced revisit time, polarimetric information, and interferometric and multi frequency capabilities have been the drivers that have conditioned recent SAR missions. Sentinel-1A/B, TerraSAR-X, TanDEM-L, TanDEM-X and Cosmo-SkyMED represent a step-up in SAR capability by achieving sub-metric resolution or implementing also new modes such as bi-static acquisitions, and providing lower revisit times by using satellite constellations.

More recently, a new trend is arising. The existence of a market demand beyond science has the emergence of actors coming from the private sector. Before that, only big space agencies developed space-borne systems due to the big investment required. Only big systems were put into orbit due to the requirements of high quality data products (fine resolution, wide area coverage). Although there are physical constraints that tie system size with resolution, some companies have bet on smaller and lower cost satellites [12]. The sacrifices in individual sensor performance are counteracted by a strong reduction in cost, which promotes the use of radar constellations. In turn, SAR constellations provide a reduction of the revisit time and an increase of the amount of data generated. This trend is called "NewSpace" [13]. It has been shown that NewSpace small satellites have in general a better performance index to mass ratio than traditional systems [13]. Two of the companies that are developing small satellite constellations are ICEYE and Capella Space. ICEYE plans a 18 satellite constellation with an average revisit time of 3 hours [14]. Capella Space aims at setting up a constellation of 36 satellites to provide 1 hour revisit time.

Nowadays, SAR has entered a maturity point that allows consistent and continued supply of data at a global scale. A prominent example of this is the Copernicus program from the European Commission. This program is meant to provide a sustained, independent space-based infrastructure for environmental monitoring, providing observations for security, climate change and the management of the environment. Currently, the space-borne segment comprises the Sentinel family of satellites [15].

Table 1.1 contains a chronological list of some important SAR systems through history and expected ones along with some of its characteristics.

Mission	Lifetime	Agency	Band	Remarks
SEASAT	1978-1978	NASA	L	1st civilian SAR
SIR-A	1981-1981	NASA	L	Technology demonstrator
SIR-B	1984-1984	NASA	L	Technology demonstrator
ERS-1/2	1991-2000 1995-2011	ESA	C	1st european SAR mission and 1st tandem configuration
JERS-1	1992-1998	JAXA	L	1st Japanese SAR mission
SIR-C/X-SAR	1994-1994	NASA DLR ASI	L C X	1st multi-frequency SAR mission
RADARSAT-1	1995-2013	CSA	C	1st Canadian SAR mission
ENVISAT	2002-2012	ESA	C	1st multi-mode SAR through antenna flexibility
RADARSAT-2	2007	CSA	C	Azim. resolution up to 1m
TerraSAR-X	2007	DLR	X	SIR-C/X-SAR and SRTM heritage
Cosmo-SkyMED	2007	ASI/MiD	X	Constellation of 4 satellites
TanDEM-X	2010	DLR	X	Tandem with TerraSAR-X and 1st bi-static SAR mission
RISAT-1	2012-2017	ISRO	C	1st Indian indigenous SAR satellite
KOMPSAT-5	2013	KARI	X	1st Korean SAR mission
Sentinel-1A/B	2014/2016	ESA	C	Constellation of 2 satellites
Gaofen-3	2016	CAST BISSE	C	1st Chinese high-resolution SAR
PAZ	2018	CDTI INTA	X	1st Spanish civil/mil. SAR Based on TerraSAR-X
ICEYE	2018	Private	X	18 small-sat constellation
Capella	2018	Private	X	36 small-sat constellation
NISAR	2022*	NASA ISRO	L S	Global ice/land deformation every 12 days
TerraSAR-X-NG	>2020*	DLR	X	3rd unit of TerraSAR-X
HRWS	>2022*	DLR	X	4th unit of TerraSAR-X
Biomass	2022*	ESA	P	Forest tomography
ROSE-L	>2028*	ESA	L	Dense temporal series with Sentiel-1

*Future missions

Table 1.1: Selection of SAR missions over time in chronological order.

1.2 GBSAR evolution

Space-borne SAR is one of the most important remote sensing techniques today. However, space systems have their own limitations. Specifically, space-borne systems are limited by its revisit time and have a limited observation geometry span of the scene. This makes space-borne SAR unsuitable for applications where real-time or near real-time observation is needed, such as in geologic or structural processes that are characterized by fast changes (e.g. landslides and infrastructure dynamics). Regarding the observation geometry, space-borne SAR is not an optimum solution when the geometry of the target scene consists of steep slopes or for more complex scenes, such as the geometries found in the mining industry. Air-borne SAR systems can serve applications that require medium revisit times and medium area coverage. However, they are still costly and have a lower limit in the revisit time, either due to cost or operative considerations. For small scale and constant measurements, Ground-Based Synthetic Aperture Radars (GBSARs) systems represent a more suitable solution. Apart from the geometric and temporal aspects, the deployment,

operation, and hardware costs of a GBSAR are significantly reduced with respect to airborne and space-borne systems. Another advantage is that there is a perfect knowledge of the sensor position, which simplifies data processing when interferometry is considered.

The pioneering GBSAR systems relied on Vector Network Analyzer (VNA) for the implementation of the radar core. A VNA is a laboratory instrument used for measuring the scattering matrix of Radio-Frequency (RF) devices, including its phase, by coherently transmitting a Stepped Frequency Continuous Wave (SFCW) signal. Their great flexibility in frequency range make them a readily available solution to implement a GBSAR system. By using a VNA, a GBSAR designer can benefit from the robustness brought by established equipment manufacturers and avoid the need to assemble custom electronics. However, the usage of a VNA comes with a set of drawbacks. First, swept frequency signal generation can be slow due to the constant re-tuning and settling times of the frequency generation system. Second, a VNA may not represent a cost-effective solution for a production stage radar due to high unit cost. Third, VNAs tend to be bulky, but at the same time need to move along with the antennas to keep the RF signal cables static. RF cable movement through the aperture would result in a time-dependent phase and amplitude distortions. The slow acquisition may be the strongest performance limiter. As the aperture time increases, effects causing loss of coherence such as atmosphere variations, vegetation or small debris movements have a stronger effect on data quality [16].

Due to the previous limitations, GBSAR manufacturers started to develop their own hardware platforms that were specially designed for being used in a GBSAR, reducing the acquisition from several minutes to less than a minute [17]. This is achieved, for example, by using different signal modulation schemes such as Linear Frequency Modulation (LFM) or Frequency Modulated Continuous Wave (FMCW).

Table 1.2 shows a selection of GBSAR systems found in the literature and the market along with its characteristics.

System	Type	Band	Pol.	Acquisition time	Scan geometry	Resolution ((m)/(mrad))
SSR-SARx [18]	?	Ku	NA	40 s	Linear	0.75/1.5
RiskSAR [19]	FMCW	X	Full	1 min (single pol)	Linear	1.25/4.4
IBIS-FM [20]	FMCW	Ku	VV	<3 min	Linear	0.5/4.3
FastGBSAR [21]	FMCW	Ku	Single/Full	4 s	Linear	0.5/4.8
MELISSA [22]	MIMO	Ku	?	2.6 ms	Motionless	0.89/21
Phoenix [23]	FMCW	X,Ku	Single/Full	?	Linear	NA
IRadar G2000 [24]	FMCW SFCW	Ku	Single	?	Linear	0.15/5.8
GB NW-SAR [25]	Noise	Ka	VV	20 s	Angular	1/12
LISA [26]	VNA	Ku	VV	35 min	Linear	2/4
NA [27]	VNA	C,X	VV,HH	?	Linear	NA
NA [28]	VNA	C	Full	?	Arc	0.25/2
NA [29]	VNA	P,L,S,C	Full	?	Linear	NA

Table 1.2: Selection of GBSAR systems in the market and literature.

1.3 Research opportunities in SAR and GBSAR system development

It is clear that the current trend in space-borne systems involves the increase of information richness by exploiting different kinds of observation diversity: bi-static configurations such as in the TanDEM-X mission or lower revisit times sought by dense constellations. As explained in Section 1.1, NewSpace is a change of paradigm with a clear directive: achieve an increase of performance-cost ratio by reducing the total development and hardware cost, while trying to maintain the value of the information delivered. This is done by employing satellite constellations that allow drastic reductions of revisit time and by exploiting the performance brought by standardized hardware components.

This directive may be relevant in the future development of other kind of systems. However, they can already be found in devices such as Software Defined Radios (SDRs). In the SDR paradigm, the advances of digital and RF technology, in part boosted by the communications mass market needs, are used to build radios capable of serving multiple communication standards through the usage of Intermediate Frequency (IF) software signal processing and flexible RF front-ends. The trends mentioned before emerge in this case: the cost reduction is achieved through the use of integrated, mass-produced hardware and the re-use of the same system for multiple applications, while trying to maintain the performance by taking advantage of advanced signal processing and hardware performance advancements.

The previous trends, along with the emergence of SDR, have been also transferred

to radar design and the term Software Defined Radar (SDRadar) has been coined [30]. SDRadar refers to a radar that operates much like and SDR by taking signal processing operations previously done in hardware to the software domain.

The research opportunity pursued in this thesis emerges from these trends. Specifically, looking at the evolution of GBSAR systems until the present day, it is natural to ask whether the common emerging paradigms found in the NewSpace sector and SDR, can be of use in the future developments of GBSAR systems. The first generation of GBSARs, as explained, used mainly laboratory instrumentation, which gave them great flexibility in frequency selection. The next generation GBSARs transitioned to custom electronics, but at the same time concentrating on single band designs, mostly at X- and Ku-band. Recovering the multi-frequency capability, but at the same time preserving the advantages of the custom electronics, may be an interesting objective to pursue. SDR, which primes flexibility, cost-effectiveness and rapid development time, could be a good fit for this goal.

Multi-frequency SAR is part of the more general group of multi-dimensional SAR techniques, such as Interferometric SAR (InSAR), Polarimetric SAR (PolSAR), their combination, Polarimetric Interferometric SAR (PolInSAR), and multi-time SAR. Multi-dimensional SAR has proven to be very useful for a wide range of applications. One of its essential characteristics "resides in the large number of available radar observables that make a better characterization of the observed terrain possible" [31]. The increased availability of space-borne SAR sensors has fostered the interest in multi-frequency data due to the varied and extensive datasets available. The frequency diversity is being exploited to improve the quality of the final products, either by selecting the most appropriate band for each scenario or by using data fusion techniques. The main advantage of multi-frequency data is the different back-scattering characteristics of each band for a given scenario. For instance, in the monitoring of landslides, while short wavelength bands such as X- and Ku-bands provide a high sensitivity to changes, their robustness is severely hindered when the terrain is covered with vegetation. In this case, longer wave-length bands, such as L-band, provide more robust results due to its higher vegetation penetration, although with less sensitivity to changes [32].

The evident advantages of multi-frequency SAR provide a reason to include this capability in the GBSAR system developed in this thesis. This capability, along with the flexibility in its configuration, is intended to give the user a versatile system that can be adapted to each scenario, and provide a means to acquire closely-spaced multi-frequency GBSAR images.

Summarizing, the main objectives of this thesis are:

1. To explore the potential use of SDR to implement a multi-frequency GBSAR system,

including X-, C-, L- and P- bands.

2. To investigate the strengths and pitfalls of using Zero-IF, the most common SDR RF hardware architecture, as part of the GBSAR system.

3. To reduce or eliminate the detrimental effects, if any, introduced by the SDR.

4. To build a first commercial prototype that presents an alternative to current GB-SARs in the market. This objective is orientated to the introduction of the system to the market. This is common in an Industrial PhD thesis, and has implications in its form and content. The thesis does not focus purely on research, but cedes part of it to more technical and implementation aspects.

5. To perform a test campaign demonstrating the capabilities of the system.

2 Background

2.1 Software Defined Radio

2.1.1 The Software Defined Radio concept

The term SDR was coined by Joe Mitola in 1992 and refers to a class of radio devices that can be reprogrammed and reconfigured [33]. An SDR can be defined as a radio device in which some or all the operations previously performed in hardware are implemented in software [34]. The idealized SDR consists on an Analog to Digital Converter (ADC) and Digital to Analog Converter (DAC) that directly samples/drives the antenna terminal, see Figure 2.1a. In this idealized concept, all characteristics of the waveform and all signal processing involved takes place in software. This idealized concept is not practical in general because the performance imposed to the digitizing devices and the software part is not achievable in practice. First, the digitizing devices should be able to work directly at RF frequencies and have dynamic ranges high enough so that no amplification in the RF domain is needed. Second, and due to these requirements, the software part should be able to cope with an enormous data rate with a huge processing load.

The idealized SDR, whilst not being practical, intends to encapsulate the idea of ultimate flexibility and marks the direction of development of practical SDR. In real scenarios, SDRs incorporate signal conditioning RF stages that adapt the signal to be digitized and generated by practical ADCs and DACs. These conditioning stages contain Low Noise Amplifiers (LNAs), Power Amplifiers (PAs), Local Oscillators (LOs), demodulators, modulators and filters. The practical SDR is shown in Figure 2.1b.

The fuzziness of the SDR definition given previously has been the origin of controversies [35]. Different views coexist on the form and extension of the software processing required to consider a radio an SDR. In other words, there are different views on the frontier between an Software Controlled Radio (SCR) and an SDR [36]. According to the Institute

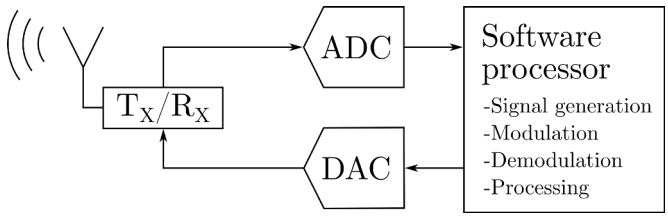

(a) Ideal SDR.

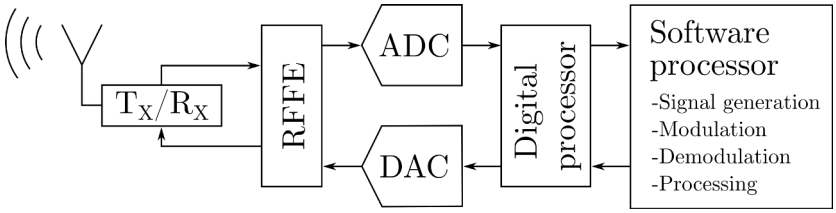

(b) Practical SDR.

Figure 2.1: Ideal vs. practical SDR.

of Electrical and Electronic Engineers (IEEE), an SCR is a type of radio where "some or all of its radio interface functions and parameters can be set or managed by software" while an SDR is "a type of radio in which some or all of the physical layer functions are software defined" [36]. In other words, a radio can be considered an SCR if some piece of software is in charge of setting radio parameters from a fixed set of possibilities, while in an SDR some or all physical layer blocks such as signal generation, modulation or demodulation are implemented in software.

The IEEE provides an explanatory note: a radio can be considered an SDR if two conditions are fulfilled:

- Some or all of the physical layer functions are accomplished through the use of digital signal processing software, or field programmable gate array (Field Programmable Gate Array (FPGA)) firmware, or by a combination of software and FPGA firmware.

- This software or firmware or both can be modified after deployment.

To clarify the previous definitions, a radio device that provides a set of fixed waveform processing functionalities which are switched by a piece of software is an SCR but not an SDR, whereas a device that provides a re-configurable and flexible way of processing this waveform is considered an SDR. Note that under these definitions an SDR is a subset of SCRs.

2.1.2 Software Defined Radio architectures

Different SDR architectures have been implemented through its evolution. Each one provides unique advantages and drawbacks by exploiting trade-offs such as processing power, complexity, cost, flexibility and integration. In general, flexibility is increased at the expense of processing power and power consumption.

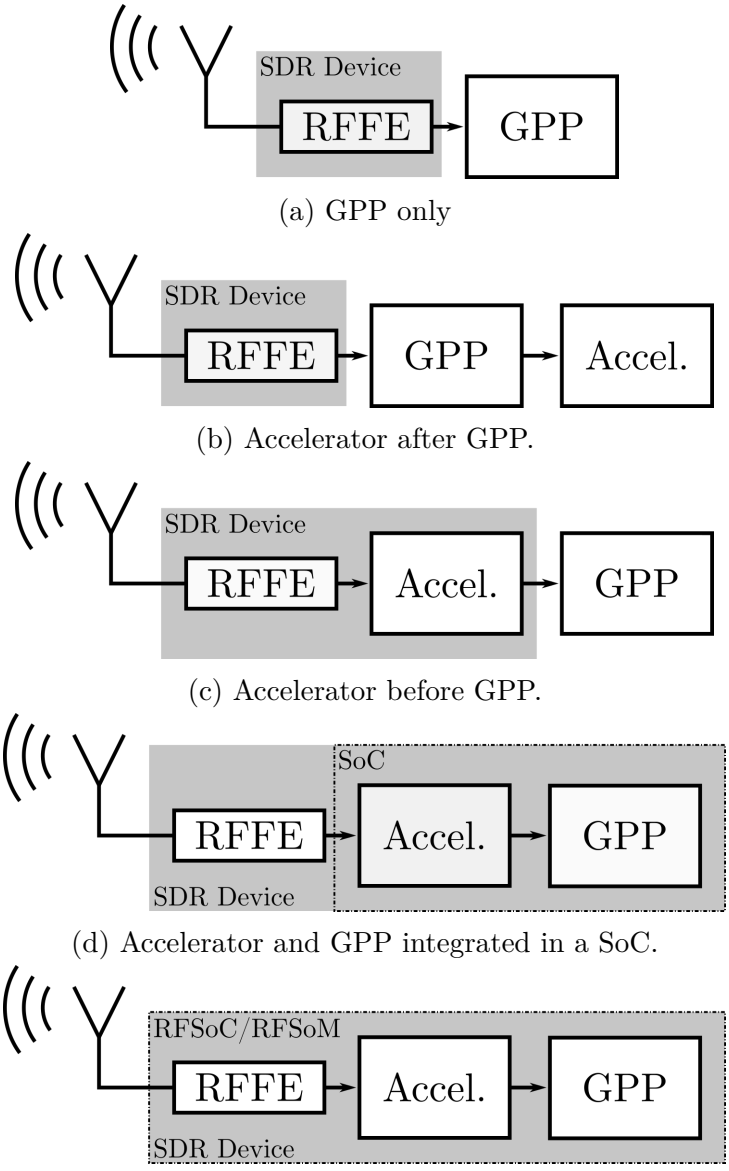

(a) GPP only

(b) Accelerator after GPP.

(c) Accelerator before GPP.

(d) Accelerator and GPP integrated in a SoC.

(e) All components integrated in a RFSoM/RFSoC.

Figure 2.2: SDR architectures.

In a traditional SDR, seen in Figure 2.2a, the RF Front-End (RFFE) interfaces to a General Purpose Processor (GPP) through a standard data interface. This is the architec-

ture that is closer to the idealized SDR and hence the one that provides most flexibility, but at the same time, current GPP implementations impose limitations in terms of signal processing capability. A GPP is usually not an optimal device for computationally intensive tasks such as correlation or filtering in real time. Parallelism techniques, such as multi-core processing or vectorized operations, are well suited for signal processing and can provide a large increase of performance. Also, the asynchronous operation of a GPP is in general not compatible with some low latency constraints.

In order to alleviate the limited processing power of GPPs, the architecture shown in Figure 2.2b makes use of a hardware accelerator consisting, in most cases, of a Graphical Processor Unit (GPU) or an FPGA. These devices are naturally well suited for true parallelism and are able to provide a large amount of data throughput at the expense of flexibility.

Even if this architecture can offload the most intensive processing tasks to a hardware accelerator, the GPP still faces the task of transferring the data from the front-end to the accelerator, and from the accelerator to itself. For high data rates, the GPP and/or the data link can become a limiter.

The architecture shown in Figure 2.2c can alleviate both problems by placing the hardware accelerator, in most cases an FPGA, between the front-end and the GPP, and interfacing it using a high speed data link. In this case, the accelerator role is two-fold: to offload a number of digital processing tasks from the GPP and, in most cases, reduce the data rate to the minimum necessary for further processing.

This architecture still relies on an off-PCB data link to transfer data to the GPP. Inter-board data links such as Universal Serial Bus (USB) or Ethernet tend to be slower and exhibit higher latency times than on-PCB data links due to signal integrity issues. In spite of the offloading provided by the hardware accelerator the data throughput between the accelerator and the GPP can be too high for this kind of links. Table 2.1 shows the maximum data rates for common data interfaces. The architecture shown in Figure 2.2d integrates the GPP in the same board or making use of a System-on-Chip (SoC).

Interface	**Host Sample Rate (MS/s @ 16-bit I/Q)**	**Half/Full Duplex**
USB 2.0	8	Half
USB 3.0	61.44	Half
Gigabit Ethernet	25	Full
10 Gigabit Ethernet	200	Full
PCI-Express (4x PCIe Card)	200	Full
PCI-Express (1x ExpressCard)	50	Full

Table 2.1: Maximum throughput for popular data interfaces. Adapted from [37].

Finally, the architecture in Figure 2.2e goes one step further by integrating the RFFE,

accelerator and GPP in the same module (Radio-Frequency System-on-Module (RFSoM)) or chip (Radio-Frequency System-on-Chip (RFSoC)).

There exists yet another architecture which is a combination of Figure 2.2c and Figure 2.2b where the acceleration is distributed between the accelerator between front-end and the GPP and another one under the orders of the GPP. It is common that the former is in charge of basic real-time signal processing while the other, usually a GPU is in charge of higher-level tasks. For instance, an FPGA could perform tasks such as decimation and filtering while the GPU could implement processing tasks on the demodulated data.

2.1.3 Processing devices

In Section 2.1.2, the processing architectures present today in SDR have been presented. This section gives an overview of the types of digital processors commonly used in SDRs.

As previously stated, a GPP is the most flexible device to implement Digital Signal Processor (DSP) algorithms. A GPP is, by design, optimized to serve the widest span of applications. The different nature of each task, however, prevents specific optimizations. Although specific hardware accelerators such as Direct Memory Accesss (DMAs) and Arithmetic-Logic Units (ALUs) offload the GPPs from common, computationally intensive tasks, such as data transfer or arithmetic operations, the GPP remains unsuitable for a high performance SDR. However, in an SDR the GPP is almost always used to perform control tasks or, when the data rate is low enough, to implement some or all the digital processing required. When the data processing effort is higher, signal processing tasks are relegated to other devices such as FPGA.

Most SDRs in the market today make use of an FPGA. One reason behind this fact is the suitability of this device to implement digital processing algorithms in parallel and its controlled latency. Also, its widespread usage in the industry favours its adoption. An FPGA is an array of logic blocks that are interconnected by the user to implement any digital circuit. Apart from logic blocks, most FPGAs include *macroblocks* that are specialized for common operations such as DSP slices, memory slices, interfaces and even complete microprocessors. The main strength of an FPGA lies on the ability to implement exactly and only the required functionality, while being re-programmable. Since the digital implementation serves a very specific purpose, power efficiency is gained in front of more flexible devices such as GPPs, because only the resources needed are used. The reason for higher signal processing power than a GPP can be found in the massive parallelism and the absence of overheads associated with GPP-like sequential operations. On the other hand, unlike GPPs, FPGAs are not naturally suited to operate sequentially and hence, are sub-optimal for control applications.

FPGAs can be classified based on the physical implementation of its logic blocks. Almost all FPGAs in the market nowadays use an Static RAM (SRAM) based architecture. The main advantage of SRAM based FPGAs is that they provide the highest block density due to the high integration of SRAM slices. However, SRAM FPGAs lose its configuration through power cycles and need to be reconfigured each time. FPGAs can also be implemented using Flash technology. Flash FPGAs provide significantly lower block density due to additional processing steps required in the manufacturing, a fact that results in these devices to lie several integration and power generations behind SRAM FPGAs. The advantages of Flash FPGAs lie in its non-volatile configuration and increased immunity against radiation. Finally, in antifuse FPGAs, the slices are connected with *antifuses*, which are one-time programmable electrical connections. Antifuse FPGAs provide the highest degree of robustness due to the immunity of antifuses to Single-Event Effects (SEEs).

Another device that has gained popularity in the SDR field is the SoC based on an FPGA in conjunction with a GPP. These kinds of devices are especially well suited when a highly integrated solution is needed. In a SoC, both devices share a common memory area so that it is especially easy to implement the interaction between both. Another advantage is that, since the communication interface between both devices resides in the chip, substantially lower power consumption and higher data rates are attainable. Examples of this kind of devices are the Xilinx Zynq-7000 or the Intel Agilex series [38, 39].

GPUs are also being introduced in the field of SDR processing. A GPUs consists of an array of floating-point multipliers optimized for array processing. GPUs implement a massive parallel processing scheme based on a programming model called Single Instruction, Multiple Threads (SIMT), which can be understood as a hybrid between vector processing and hardware threading. GPUs can outperform GPPs in terms of processing power by an order of magnitude when high amounts of data can be parallelized for processing. One important consideration is that GPUs can lose its potential when the amount of data is low due to overheads in incoming and outgoing data transfers. Programming interfaces available for GPU programming are CUDA and OpenCL, being the former proprietary and available only for NVIDIA devices and the second open-source. Another consideration is that GPU programming is non-intuitive. Libraries such as Numba [40] hide some of its complexity by providing implementations for the most common operations, for example the Fast Fourier Transform (FFT). Finally, it is important to state that in most cases, data transfers from and to the GPU are managed by the GPP. This is a sub-optimal implementation because the GPP spends a significant amount of resources only for data routing, degrading latency and throughput. Very recent developments such as NVIDIA GPUDirect [41] target this issue, by allowing direct access of the GPU to the data interface.

Other devices, such as specialized processors for SDR, Application Specific Integrated Circuits (ASICs) or DSPs are not considered here because they serve a niche in the SDR industry and are out of scope of this thesis. In fact, most specialized SDR devices have failed commercially [42].

2.1.4 SDR RF front-end architectures

Historically, the superheterodyne architecture (Figure 2.3) has dominated radio design [43]. With careful frequency planning, this architecture allows exceptionally low spurious levels. In the superheterodyne architecture, the incoming signal is mixed with an LO signal in order to produce an IF signal, which is then processed. In this topology, the most stringent filtering requirements are done at IF rather than RF. Filtering at IF relaxes the filter quality factor requirements and allows using high performance IF filters, which are common in the market. For enhanced spurious levels, multiple mixing-filtering stages can be chained. This is called the multistage (or high order) superheterodyne architecture. This last architecture delivers enhanced image rejection due to relaxed RF filter requirements and higher linearity due to gain distribution between the multiple stages.

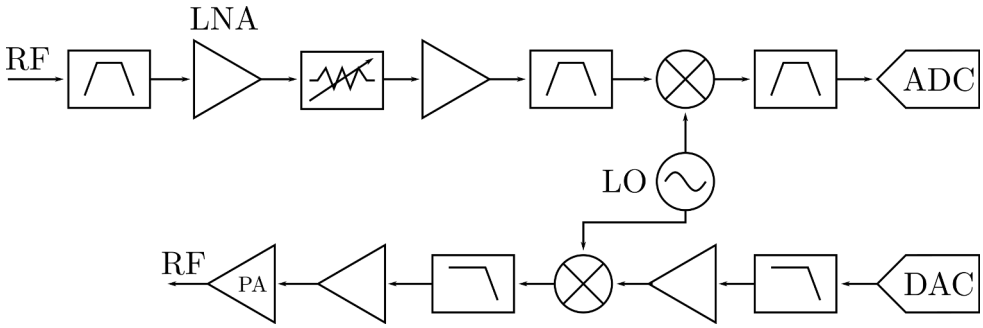

Figure 2.3: Simplified typical superheterodyne transceiver.

However, the performance of superheterodyne architectures comes with a set of drawbacks. First, the electronic part count is high and so is the cost and power consumption. Second, the low spurious content is achieved only within a limited frequency range, a fact that limits the tuning range. Specially in high order mixers, frequency re-tuning can result in complex interactions between multiple components which make frequency flexibility particularly difficult to achieve. In general, the simpler the architecture the more predictable its performance is. Finally, the superheterodyne topology is not well suited for physical integration. While some components can be integrated in a single chip, for instance gain stages and mixers, the parts required for the filtering stages are difficult or impossible to integrate. The reason behind that is the difficulty in manufacturing some de-

vices in Complementary Metal-Oxide-Semiconductor (CMOS) or other planar Integrated Circuit (IC) technologies. This includes, for example, large value inductors, capacitors and Surface Acoustic Wave (SAW) filters. In an integrated chain, this would mean that every time a signal needs to be filtered it must be routed off-chip to external filters and routed back in. Doing so would impose a performance burden due to signal integrity losses each time the chip interface is crossed.

The combination of the superheterodyne drawbacks and the market needs outlined at the beginning of the section have promoted the adoption of the Zero-IF or direct conversion architecture. The Zero-IF architecture, seen in Figure 2.4a and 2.4b, "has proven to be the lowest cost, the lowest power and the smallest footprint solution in any radio technology" [44]. The Zero-IF architectures removes all components that cannot be integrated (mainly IF filters and IF amplifiers) and is able to provide true broadband capability. This architecture, however, has not been the choice of many designs due to the low performance achieved in terms of image rejection and other inherent effects such as LO leakage. Many of these impairments have been greatly improved due to a combination of manufacturing processes, design and digital algorithms, partly motivated by the market push.

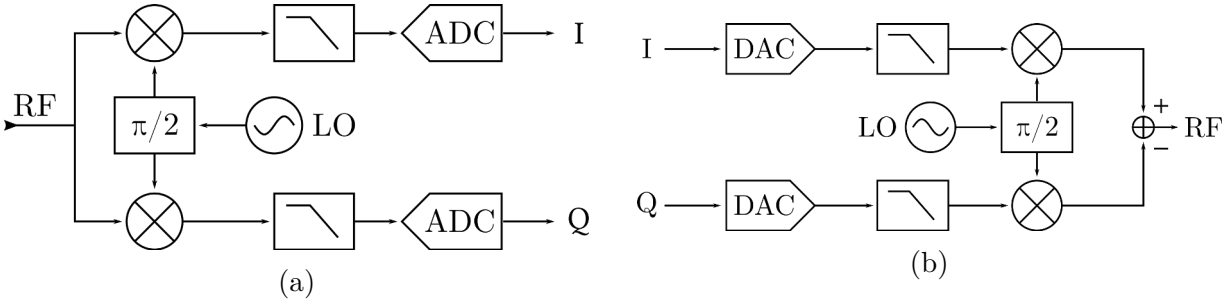

Figure 2.4: (a) Zero-IF receiver architecture. (b) Zero-IF transmitter architecture.

A Zero-IF receiver[1] uses a single mixing stage with it LO tuned directly at the carrier frequency, translating the RF signal directly to in phase (I) and quadrature (Q) components. In the simplest configuration, an LNA precedes a mixing stage consisting of two mixers whose LOs are shifted by 90^{o}. After the mixers, low-pass filters in each branch provide the required frequency selectivity. The fact that selectivity is achieved through low-pass filters is a very relevant fact for two reasons: they can be easily integrated and can be electronically tuned in the range from hundreds of kHz to hundreds of MHz, allowing instant changes in bandwidth without any change in hardware. The goal of these filters is

[1]The discussion centres on the receiver chain for the sake of simplicity and is analogous to the transmitter.

to eliminate the image tone as a result of the mixing process and remove frequency content beyond the sampling rate of the ADCs to prevent noise and other signals to fold into base-band. Finally, a very relevant feature of the ideal Zero-IF is the absence of RF image frequency [45]. This can be understood either by an inherent image reject capability of the frequency conversion procedure, or the fact that complex signals, instead of real ones, are used for frequency conversion. Section **??** shows that, in practice, the image rejection is not infinite due to non-idealities.

Regarding the naturally broadband capability of Zero-IF receivers, this feature comes from the relaxed frequency planning restrictions with respect to super-heterodyne architectures. This is because the image frequencies are inherently reduced by the IQ down-conversion technique, regardless of the frequency, contrary to the super-heterodyne architecture, where image rejection is performed through fixed filters. Also, while in this last configuration the designer must account for various mixer spurs such as the particularly troublesome half-IF frequency [46], in the former the problems related to mixer spurious content are much less severe [45].

The simple architecture and higher integration of the Zero-IF architecture has a profound impact in cost reduction. Regarding integration, the reduced part count and absence of discrete element filters lead to layout area reductions around by 50% [44]. The reductions in cost originate from various aspects from design to manufacturing. As stated, the first contributor is the reduced part count. The reduced Printed Circuit Board (PCB) layout also has another consequence in the manufacturing process because higher factory yields are expected for smaller PCBs. Another contributor is the reduced engineering effort due to simpler design and the increased re-utilization of the same design (due to the inherent broadband capability) for a wide span of applications. Finally, the manufacturing benefits from the integration (mainly the filters) due to reduced device to device variability. Although difficult to asses, cost savings on the order of 30% at system level are estimated [44].

2.2 Ground-based Synthetic Aperture Radar

2.2.1 Types of GBSAR

The simplest and most used GBSAR, illustrated in Figure 2.5a consists on a coherent transceiver unit mounted on a linear rail. In this configuration, the radar unit transmits and receives at specific points of this linear unit, synthesizing a linear array antenna. The length of the rail determines the resolution in azimuth, so the longest rail within practical

bounds is normally used. This length lies in most cases around two meters. The scene extension sensed by a linear GBSAR is limited by the antenna Field of View (FOV). In situations where an area to be sensed is wider than the FOV this is may a limiting factor. An example of this situation could take place, for example, in an open-pit mine.

Circular GBSAR [47], illustrated in Figure 2.5c addresses this limitation by performing a circular aperture that provides 360º coverage. An important benefit of this system, contrary to linear GBSAR, is that it provides a constant angular azimuth resolution. A disadvantage is that a defocusing effect occurs for targets far from the rotation plane [48].

Finally, Massive Input Massive Output (MIMO) GBSAR [22, 49–52], illustrated in Figure 2.5b offers a technically attractive alternative since it does not use mechanical moving parts, which are prone to failure. In MIMO GBSAR, the synthetic array is made from multiple antennas strategically positioned in space. For N_{TX} and N_{RX} transmit and receive elements, a synthetic array of $N_{TX} \times N_{RX}$ points can be formed. The main disadvantage of MIMO GBSAR is the cost associated with the high computational power required.

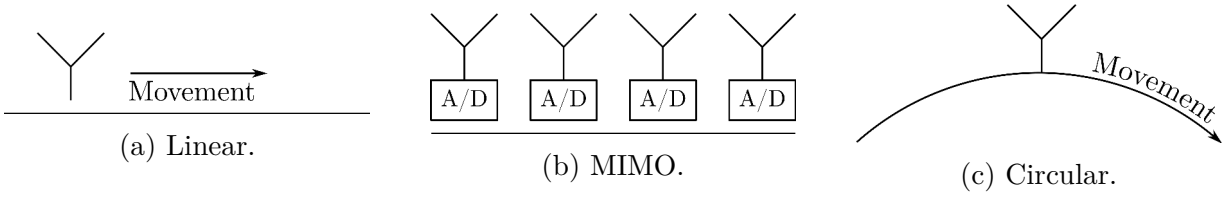

(a) Linear. (b) MIMO. (c) Circular.

Figure 2.5: Types of GBSAR.

2.2.2 Overview of GBSAR imaging

Range domain description

The ranging capability of a radar is achieved by exploiting the comparison of the transmitted and the received signal. In pulsed systems, ranging is performed by a measurement of the round trip delay of the pulse. The range resolution of a radar employing a monochromatic pulse is linearly dependent on the duration of the pulse. The resolution can be increased through the use of a certain modulation to the signal and using a matched filter or the pulse compression technique on receive [53].

Consider a set of point targets with an Radar Cross Section (RCS) equal to σ_n and phase ϕ_n located at a certain range x_n from the radar. This is described by the range profile function:

$$f_0(x) = \sum_n \sqrt{\sigma_n} e^{j\phi_n} \delta(x - x_n) \tag{2.1}$$

Which can be linearly mapped to the time domain via:

$$x = \frac{ct}{2} \tag{2.2}$$

where c is the speed of light and the factor of two accounts for the round trip delay. Defining $p(t)$ as the codification of the pulse, the received signal can be expressed as the sum of the echoes resulting from each target:

$$s(t) = \sum_n \sqrt{\sigma_n} e^{j\phi_n} p\left(t - \frac{2x_n}{c}\right) = f_0\left(\frac{ct}{2}\right) * p(t) \tag{2.3}$$

The matched filtering operation is described as follows [53]:

$$s_M(t) = s(t) * p^*(-t) = f_0(\frac{ct}{2}) * \mathrm{psf}_t(t) \tag{2.4}$$

$$\mathrm{psf}_t(t) = \mathcal{F}^{-1}_{(\omega)}\left[|P(\omega)|^2\right] = p(t) * p^*(-t) \tag{2.5}$$

Where $\mathcal{F}_{(\omega)}$ is the Fourier transform operator, $P(\omega) = \mathcal{F}_{(\omega)}$ and $\mathrm{psf}_t(t)$ is referred to as the Point Spread Function (PSF) in the time domain. The PSF determines the signature of a given target in the time or range domain, after matched filtering. The spectral properties of the transmitted signal are directly related to the shape of the PSF. In particular, the bandwidth B_0 of $P(w)$ determines the spread of the PSF in the range domain, hence determining the range resolution. A first order approximation of the range resolution is given by:

$$\delta_x = \frac{c}{2B_0} \tag{2.6}$$

Increasing the pulse bandwidth can be done either by reducing its duration in time domain and/or by modulating the pulse. LFM is the most popular technique due to its simplicity. An LFM pulse has a linearly increasing frequency such that

$$f(t) = \beta + \alpha t, \tag{2.7}$$

where β is the carrier frequency and α is the frequency increase rate, called "chirp rate" or "sweep rate", and is defined as the product of its frequency span, BW, and its Pulse Repetition Frequency (PRF). Then, by integrating the frequency, the LFM pulse can be expressed as

$$p(t) = a(t)e^{j\beta t + j\frac{\alpha}{2}t^2} \tag{2.8}$$

$$a(t) = \prod\left(\frac{t - T_p/2}{T_p}\right), \tag{2.9}$$

where $\prod(t)$ is the normalized boxcar function, T_p is the pulse duration. The bandwidth of an LFM pulse is in a good approximation equal to $2\alpha T_p$, provided that $2\alpha T_p \gg (2\pi)/T_p$ [54]. Note that the bandwidth of an LFM pulse increases with pulse duration, contrary to the monochromatic pulse. This fact is known as *pulse compression* and is widely exploited in radar systems [6]. Pulse compression offers the notable advantage of spreading the signal energy through a longer time, reducing the required instantaneous power and relaxing hardware requirements.

LFM signals are well suited for another form of range reconstruction called deramping or dechirping. This is the method used in by the FMCW technique. In the deramp method, the received signal is mixed (multiplied) by another LFM signal which is in most cases a replica of the transmit signal:

$$\begin{aligned} s_c(t) &= s^*(t)\underbrace{\exp\left(j\beta t + j\frac{\alpha}{2}t^2\right)}_{\text{Reference}} \\ &= \sum_n \sigma_n a^*\left(t - t_n\right)\underbrace{\exp\left(j\beta t_n - j\frac{\alpha}{2}t_n^2\right)}_{\text{Undesirable phase}}\underbrace{\exp\left(j2\frac{\alpha}{2}t_n t\right)}_{\text{Sinusoid}} \end{aligned} \tag{2.10}$$

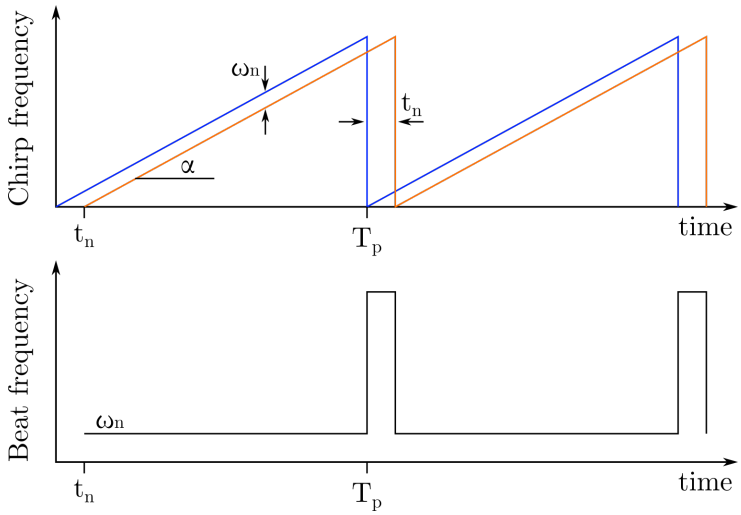

Figure 2.6: Deramp technique. The blue and orange signals are the transmitted and the received one, respectively. Amplitude factors are ignored for convenience. The beat frequency is equal to the frequency difference between both chirps.

The range information of a given target is contained in the sinusoid frequency $\omega_n = 2\alpha t_n$, called the beat frequency. The dechirping method is illustrated in Figure 2.6. Given

a round-trip delay $(2 * x_n)/c_0$, where x_n is the range of the n-th target, it can be written that the mapping between the beat frequency ω_n and range is:

$$x_n = \frac{c_0 \omega_n}{2\alpha} \tag{2.11}$$

Note in Figure 2.6 that the beat frequency suffers an undesired peak at the end of the transmitted chirp with a duration of t_n. This peak is removed either in post-processing or by using guard times before recording the signal. Also, the signal contains an undesirable phase term that must be removed to avoid undesired effects in further processing such as Synthetic Aperture Radar (SAR) focusing. The term αt_n^2 is known as the Residual Video Phase (RVP).

In this case the PSF and the range resolution are [53]:

$$\text{psf}(x) = \mathcal{F}_{(t)}\left[a^*(t)\right] \tag{2.12}$$

$$\delta_x = \frac{\pi c_0}{2\alpha T_p} \tag{2.13}$$

Since $s(t)$ is a rectangular pulse, the PSF is a *sinc* function. Note that the range resolution is identical in the matched filter case.

The compensation of the RVP is done by multiplying the received signal in the frequency domain with a compensation function $F[m]$ [55] so that

$$S_c^{RVP}[m] = S_c[m]F[m], \tag{2.14}$$

$$F[k] = e^{j\alpha\left(\frac{\Delta w m}{2\alpha}\right)^2} \text{ for } m = 1, 2, \ldots, Nf_z, \tag{2.15}$$

$$\Delta\omega = \frac{\omega_S}{Nf_z} \simeq \frac{2\pi}{T_p f_z}, \tag{2.16}$$

where $\omega_s = 2\pi/T_p$ is the sampling angular frequency, m is the range index of the sampled data in the frequency domain, Δw is the frequency separation between indexes, f_z is an interpolation factor resulting from zero-padding in time domain and N the number of samples in the chirp without interpolation. Interpolation in the frequency domain is necessary to reduce the quantization error that arises when a given target range is not an exact multiple of $\Delta\omega$. It has been shown that for low range radar systems, the quantization error is negligible for $f_z \geq 16$ [55].

Cross-range domain description

While the range domain is related to the round-trip delay of the transmitted signal, which propagates at the speed of light, the cross-range domain is related to the phase evolution of the signal as the platform moves in time. Range domain is equivalently referred to as the *fast-time* domain because the delay are measured using signals propagating at light speed, while the cross-range domain is referred to as the *slow-time* domain, since the phase changes are due to the much slower platform speed.

In order to give an overview of GBSAR imaging, it is beneficial to briefly state some properties of conventional SAR. In conventional SAR, a side-looking antenna mounted on an aerial or space platform illuminates the target scene [5]. Stripmap SAR with a planar antenna is considered here for illustrative purposes for its simplicity. In stripmap SAR, the antenna is looking perpendicular to the flight path. Considering a planar antenna with length D_y, its beam-width ϑ_y in cross-range is $\vartheta_y \approx \frac{2\lambda}{D_y}$, where λ is the signal wavelength. The antenna illuminates a given target during the full time it is within the antenna beam, being it proportional to the antenna beam-width ϑ_y, and hence to λ. By processing the phase history of the received signal throughout the synthetic aperture, a stripmap SAR is able to image an area with a cross-range resolution $\delta_a = \frac{D_y}{2}$ [53]. This is the most significant result of SAR imaging, since it shows the independence of the cross-range resolution from the signal frequency and platform height. The origin of this independence comes from the fact that, in the cross-range domain, the spatial resolution is inversely proportional to the bandwidth B_y of the signal in the wave-number domain[2]. B_y is defined as the frequency occupation of the signal in the spatial frequency domain. It can be shown independent on height as long as the target is illuminated throughout the full cross-range aperture span. B_y can also be shown to be independent of λ under the same condition [53]. In other words, in stripmap SAR, the synthetic aperture equals the cross range span of the antenna beam.

In GBSAR systems, on the other hand, the full cross-range antenna beam span is not used to illuminate a given target due to the limited synthetic aperture length. This has a profound impact on the resulting image, by introducing a range and azimuth dependence on the azimuth resolution, that worsens for higher range and azimuth angle. Figure 2.7 illustrates this difference. A full discussion of this effect can be found in Pipia [55] and the most important results are summarized here.

Using the geometry depicted in Figure 2.8, and defining $u \in [-L/2, L/2]$ as the position

[2]In the wave-number domain, functions are dependent on the spatial variable x, which in this case is a range distance. The frequency counterpart of x is k_x, called spatial frequency domain or wave-number domain, and its units are *rad/m*

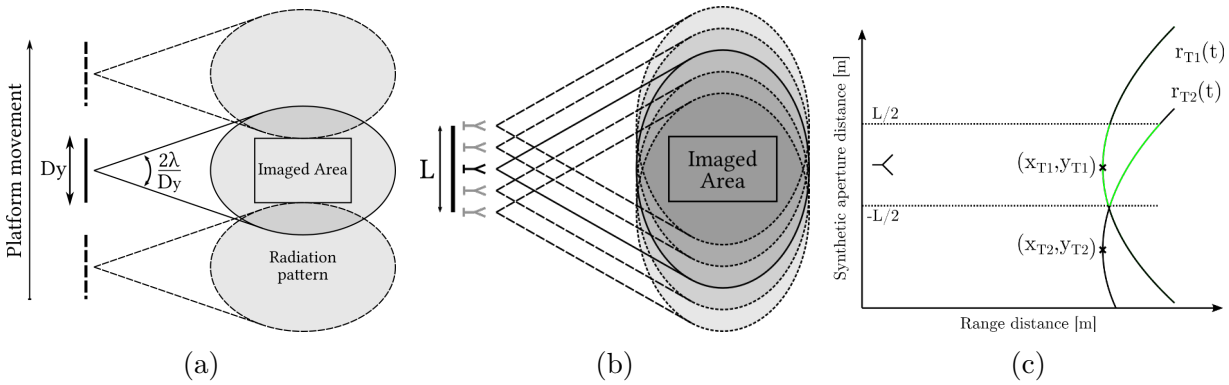

(a) (b) (c)

Figure 2.7: (a) Stripmap SAR configuration. The target area is illuminated throughout the full radiation pattern span. (b) Linear GBSAR representation. The synthetic aperture is much shorter than the imaged area. (c) Range history of two targets located at different cross-range. A GBSAR is able to use a limited portion (green) of the range history that would be used in an airborne or space-borne SAR.

of the radar platform within the aperture, the range of a target located at the point (x_T, y_T) across the aperture is:

$$r_T(u) = \sqrt{x_T^2 + (y_T - u)^2} \tag{2.17}$$

At $u = y_T$, the range is minimum and equals x_T. The aspect angle $\vartheta_T(u)$ is given as:

$$\vartheta_T(u) = \arctan\left(\frac{x_T}{y_T}\right) \tag{2.18}$$

Given a target, the recorded signal along the aperture, after fast-time baseband conversion, can be defined as:

$$s_T(u) = \sigma_n \exp\left[-j2kr_T(u)\right], \tag{2.19}$$

where $k = 2\pi/\lambda$ is the wave-number or wave spatial frequency. The phase term is referred to as the phase history. The bandwidth of the phase history in the wave-number domain, for an infinite aperture and isotropic, antennas is given by

$$\Omega_T = \left[-2k\sin\vartheta_T\left(\frac{L}{2}\right), 2k\sin\vartheta_T\left(-\frac{L}{2}\right)\right]\Big|_{L\to\infty} = [-2k, 2k], \tag{2.20}$$

where L is the synthetic aperture length and. In real cases the phase history is limited either by the antenna radiation pattern or by the limited aperture. The azimuth bandwidth becomes

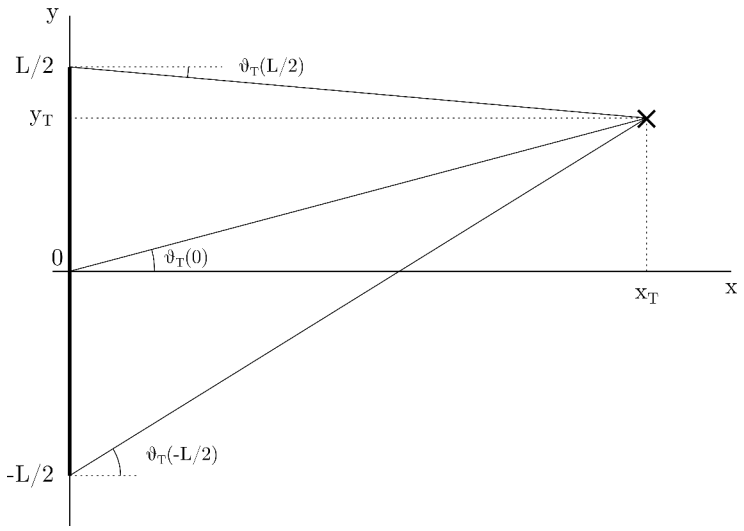

Figure 2.8: Bi-dimensional geometry of a GBSAR scene.

$$\Omega_T = [2k \sin \vartheta_{\text{TMAX}}, 2k \sin \vartheta_{\text{TMIN}}] \,, \tag{2.21}$$

where ϑ_{TMAX} and ϑ_{TMIN} are the maximum and minimum aspect angles. In the case of a stripmap acquisition, ϑ_{TMAX} and ϑ_{TMIN} are given by $-\vartheta_y/2$ and $\vartheta_y/2$, respectively. In this case, and considering rectangular aperture antennas, the bandwidth simplifies to:

$$\Omega_T = \frac{4\pi}{L} \tag{2.22}$$

And the cross-range resolution is roughly estimated as

$$\delta_a \approx \frac{2\pi}{\Omega_T} = \frac{L}{2} \tag{2.23}$$

In the GBSAR case, and considering a target located at a range x_T and aspect angle $\vartheta_T(0)$ as with respect to the radar platform at the middle of the aperture, its phase history is not necessarily symmetric and it becomes a pass-band signal centred at

$$\Omega_{TC} = 2k \sin \vartheta_T(0) \tag{2.24}$$

and has a total bandwidth of

$$\Omega_T = \frac{2kL}{x_T} \cos^2 \vartheta_T(0), \tag{2.25}$$

which leads to a cross-range resolution given by

$$\delta_a \approx \frac{2\pi}{\Omega_T} = \frac{x_T \lambda}{2L\cos^2\vartheta_T(0)} \tag{2.26}$$

This result shows how the cross-range resolution worsens with range and azimuth angle. Note that the best cross-range resolution is achieved when $\vartheta_T(0) = 0$. Alternatively, the azimuth resolution is given in terms of angular resolution. For low aspect angles the angular resolution is approximated by dividing δ_a by the target distance $x_T/\cos(\vartheta_T(0))$ so that:

$$\Delta\vartheta \approx \frac{\lambda}{2L\cos\vartheta_T(0)} \tag{2.27}$$

2.3 Bibliographic review

One of the first authors that discussed the SDRadar idea is Werner Wiesbeck [30]. In his paper, the developments of air-borne and space-borne SAR systems since their beginnings are discussed, and the deficiencies of the then State of the Art (SoA) SAR systems are emphasized. From his point of view, the technical developments achieved in SAR technology, notably the use of phased array antennas, were made possible by increasingly complex hardware systems. This complexity, however, generated some side effects, including: bulky systems, decreased reliability, low efficiency and difficult calibration. In order to mitigate these deficiencies, a new system architecture, called SDRadar, was proposed. The author envisioned a SAR in which all operations are software controlled, meaning that not only certain parts of the hardware are controlled by software, but that there is full control on the transmitted and received signals. This system, could transmit any type of code, and even be used for communication purposes. The goals of this architecture, as previously stated, are to solve the deficiencies of SoA SAR systems by providing less complexity, lower cost, higher flexibility, lower weight and higher efficiency. Finally, it was proposed that the emerging SDR technology could facilitate the implementation of the SDRadar concept.

From the inception of the SDRadar concept, many authors have explored it, and successful implementations have been reported. What follows is a brief review of them.

One of the first successful implementations of an SDRadar can be found in Patton [56]. In this work, an SDRadar prototype based on the Universal Software Radio Peripheral (USRP) is implemented. A commercial SDR based on an Altera Cyclone FPGA and a commercial 2.4 GHz transceiver are used. While time coherence is not found to be a problem, time synchronization between transmission and reception signals is not achieved

by the USRP, therefore synchronization scheme based on the usage of a preamble signal and the front-end leakage between transmit and receive ports is proposed. The time synchronization issue discussed by the authors was a common problem in the first generation USRP, while newer architectures solve this issue through timed commands that can instruct the SDR to perform actions such as transmit and receive exactly at a specific time [57]. The synchronization issue in USRP radios is discussed more in detail by Aloi et al. [58], where the same scheme presented in Patton [56] is used and preamble optimization is discussed.

MIMO radar is becoming an active research topic because of its versatility and can be considered a subset of the more general SDRadar concept. A MIMO radar benefits from early digitization of the signal at each antenna element, shifting the complexity from RF hardware, e.g. phased arrays, to digital processing. Although the digital system of a MIMO is more complex than a phased array, mainly due to the multi-channel design, it benefits from increased flexibility. SDRs have provided a natural way of implementing the transceiver chain of each MIMO channel. In Frankford et al. [59], a MIMO radar test-bed is implemented using a custom SDR built from commercial DSP and FPGA boards along a custom RF front-end. Mealey et al. [60] introduces a software-defined test-bed aimed at MIMO development and verification. The benefits of using commercial SDRs are emphasized regarding the faster and easier system development. It is also pointed out that the conventional way of processing the base-band information in SDRs, i.e. in a GPP, does not scale well due to the high computational demand, that scales linearly according to the number of array elements. In order to reduce this burden, the system is configured as a heterogeneous multiprocessor, where some computationally intensive processing tasks are pushed into the SDR hardware, i.e. in its FPGA. The author proposes RF Network-on-Chip (RFNoC), a networked signal processing scheme, as an implementation scheme for his task. RFNoC [61] plays an important role later in this thesis since it is used in the FPGA digital implementation.

The flexibility of SDRs is demonstrated in Petri et al. [62], where a passive USRP based radar using UMTS signals is implemented. Its potential applications include short range urban traffic monitoring.

Another early investigation the potentialities of SDRadar can be found in Rossler et al. [63]. In this case, the versatility of SDR is exploited to create a joint radar-communication system. The system uses wide-band signals used in communications to simultaneously sense its backscattering from a given scene.

SDRs have been also employed for environmental research. Nagarmat et al. [64] describe a system for atmospheric research. In this case, four USRP radios are used for receiving the back-scattered signal at different points in space to exploit interferometric

techniques for meteor sensing. A radar controller provides trigger signals to a custom pulse radar transmitter and a hardware trigger signal to specify the receiver signal window to each radio device, effectively achieving time synchronization. Bostan et al. [65] use a similar system for the study of the ionosphere. A Direct Digital Synthesizer (DDS) is used for pulse waveform generation in conjunction with a transmit RF front-end and a radar controller, while a first generation USRP is used as a receiver. Transmit and receive synchrony is achieved using a hardware trigger signalling both the DDS and the SDR. More recently, the uses of a USRP-RIO platform for polar-ice sheet research has been described in Liu et al. [66]. The USRP-RIO is powered by the LabVIEW Reconfigurable I/O (RIO) architecture.

Costanzo et al. [67] use a USRP NI2920 to implement an L-band radar. This system is based on a mechanical scan system aimed at providing landslides monitoring in the presence of vegetated areas. It is one of the first publications where 1G Ethernet data interface between SDR and the host computer is exploited. The improved data bandwidth with respect to previous systems allows using a wider band signal, leading to an increased range resolution of 6 meters. This is significantly better than previous works, where USB was used. Spadafora et al. [68] uses the same system at P-band making a performance evaluation, comparing the superior target range resolution of the USRP NI2920, with respect to a first generation USRP. It demonstrates the system flexibility by using the same system as an FMCW or Orthogonal Frequency Division Multiplex (OFDM) radar. Costanzo et al. [69] show a real use case, where the developed L-band SDRadar is part of an integrated system for landslide monitoring.

Kwag et al. [70, 71] present a multi-band and multi-mode SDR radar. The system uses a replaceable RF front-end module with S- X- and K-band versions. A processor module which can be considered an SDR consisting on two FPGAs, an ADC, a DAC and a system controller is in charge of waveform generation and receive pre-processing processing. The transmit waveform is generated with a DDS and can be a pulse, Continuous Wave (CW), an FMCW or an LFM pulse. Pre-processing tasks include digital down-conversion, a Hilbert transform and digital pulse-compression or dechirp. The host computer can configure the system through the system controller and receive the data from one of the FPGAs for higher level processing. As a real-world example, the author shows a drone detection scenario at K-band.

Pancik et al. [72] present a low cost FMCW SAR system employing an USRP N210 and a custom RF front-end. The front-end includes a DDS for signal generation. The SDR is used for digitizing and pre-processing the signal, as well as providing control signals to the RF front-end. Using the FMCW technique along with a dedicated DDS is a way to circumvent the data throughput bottleneck described in previous works and allows a high

range resolution (1 m) to be achieved. Hardware dechirping relaxes the receive sampling requirements, while using an external DDS allows higher transmission bandwidths than the N210 SDR can provide. Grabowski et al. [73] show another high resolution SAR. The signal is generated with a DDS, but in this case, the synthesizer is implemented in the FPGA, achieving a bandwidth of 40 MHz, which is later extended to 960 MHz through a multiplier in an external RF front-end.

SDRadar has also found applications in the medical field. Marimuthu et al. [74] describe an SDRadar for near-field medical imaging with a BladeRF SDR in its core. In this case, a virtual ultra-wideband time-domain pulse is synthesized by coherently adding multiple frequency spectrums together. Since the SDR uses different frequency synthesizers for trasmit and receive, coherency is achieved through the use of a phase recovery scheme that senses the phase after each synthesizer re-tune.

Hershberger et al. [75] describe a dual-polarization, continuous-wave, mono-static, software-defined radar system, based on the Ettus Research USRP-B210 SDR. The transmit and receive channels make use of different frequency synthesizers, so a phase calibration is performed before the start of each acquisition. The signal generation is offloaded to the SDR FPGA, which stores the waveform in a Read Only Memory (ROM) block and transmits it on demand. This is an alternative to generating the waveform using a DDS that can be more flexible depending on hardware resources and waveform length. In Hershberger et al. [76], the same author investigates the performance of the USRP B210 and the USRP X310 with UBX-160 daughter-boards in terms of phase coherence and signal isolation, both in single and dual SDR designs and using the same phase calibration technique in its previous paper. It is found that all configurations offer a viable implementation of dual-polarized radars, being channel to channel or board to board isolation the main concern in single SDR systems and phase coherence the one in dual SDR ones.

SDR has also found its way into cognitive radar. Kirk et al. [77] presents a cognitive radar with spectrum sensing able to select Radio-Frequency Interference (RFI) free frequency intervals. LabView, is used for signal generation and processing. The radar is based on an USRP X310 and UBX-160 daughter-boards, for which the author provides a detailed RF performance analysis. In a later publication, [78] uses the FPGA Block Random Access Memory (BRAM) to store the TX waveform. Time synchronization is achieved by using the pulse per second (PPS) input, which is configured to act as a trigger. The author details the RFI avoidance technique, where the ambient spectrum is sensed and the transmission (TX) waveform (and consequently the matched filter) is designed on the fly to avoid RFI regions. Finally, the versatility of the SDR is demonstrated again by the use of waveform adaptation for clutter suppression.

In the last years, some authors have used methods for expanding the bandwidth ca-

pabilities of existing SDRs. A frequency stacking method is provided in Carey and Waymond [79] for its usage in a Ground Penetrating Radar (GPR). In this method, the author uses a multi-tone signal to take advantage of the instantaneous bandwidth, while re-tuning the local oscillators to expand the effective bandwidth to cover the full range offered by its SDR (500-5000MHz). In this case, time synchronization and phase coherence is achieved through timed commands, which trigger Phase-Locked Loop (PLL) phase synchronization events and data transmission and reception synchronously. Prager et al. [80] use an Ultra Wide Band (UWB) synthesis technique to implement a high range resolution radar. In this case LO re-tunes are used in conjunction to an RFNoC signal generator to create a set of overlapped LFM chirps that cover the full frequency range of the SDR. The chirps are then combined to synthesize a high bandwidth, which leads to a range resolution on the order of few centimetres. These last two publications contain two elements important to the present thesis: timed commands and the usage of RFNoC for signal generation. These two concepts are used for signal time synchronization and full bandwidth signal generation and processing.

Vidal-Morera [81] addresses the simulation of an FMCW radar system considering the usage of an USRP X310 SDR and a UBX160 daughter-board from Ettus Research. This is the configuration chosen for the present thesis. The simulations demonstrate that the system, used as is, is capable of achieving a performance comparable to most GBSAR sensors developed. In the discussion, the author concludes that it would be beneficial to perform dechirping on hardware rather than in the host computer, due to the reduced sampling rate necessary. This publication, is one of the motivators for the realization of the present thesis. In what follows, a continuation of the idea presented in the paper is described, and an attempt to implement a working GBSAR prototype based on SDR technology is presented.

3 System description and development

This part is omitted due to non-disclosure agreements.

4 System tests and results

The objective of this chapter is to evaluate the system operation, to demonstrate its capabilities in real scenarios and to show its results. Throughout the development of this thesis, extensive testing has been part of an agile design cycle. Small and progressively more complex tests have been carried out to validate different aspects of the GBSAR operation, such as signal generation, acquisition, RFI, leakage cancellation and image formation, among others.

4.1 Early tests

One of the early developments was the implementation of a single frequency modular front-end. The unit consisted in individual RF component custom assemblies that allowed rapid experimentation either in the laboratory or directly in an outdoor test site. The configuration was set for X-band most of the time in order to keep the complexity manageable, by avoiding most switching electronics and most filtering stages. The assembly was inside a compact enclosure, which also enclosed the SDR. The antennas were commercial, low-cost models consisting on metallized plastic horns, which connected to a wave-guide to SubMiniature version A (SMA) transition.

The first tests were aimed at validating the real aperture mode, by performing static acquisitions of various scenes containing Trihedral Corner Reflectors (TCRs) and other clearly visible targets. Testing followed by mounting the assembly on a one-metre photographic linear unit, which had enough stability and length to experiment with the formation of the first SAR images. Sample pictures of these tests can be seen in Figure 4.1. These tests allowed to discover some problems in the system operation. For example, inconsistent Ethernet latency, due to the use of a virtualized interface [1], prevented some

[1] A virtualized interface is an emulation of a hardware component, in this case an Ethernet interface.

(a) RAR test (b) Early SAR configuration

Figure 4.1: Early RAR and SAR mode tests.

acquisitions to be finished due to sample packets being lost. This was an indication that the link quality between the SDR and the host was of utmost importance, and allowed a very robust operation when a physical interface was used. Another problem indicated by early testing was the presence of a broadband spur in the real aperture mode, or equivalently, a zero azimuth spur that rendered the image quality unacceptable, as seen in Figure 4.2a. It was determined that this spur appeared due to imbalance effects in the Zero-IF SDR architecture. Initially, it was thought that a better imbalance compensation would be sufficient to eliminate the spur, however, the reduction in spur power was not strong enough to compensate for the high processing gain of later stages. This led to the need to completely remove it, and the application of the Super Spatial Variant Apodization (SSVA) reconstruction algorithm described in Section **??**, and which result is shown in Figure 4.2b. In later campaigns, the Short Time Fourier Transform (STFT) method was also investigated and implemented due to the ineffective reconstruction of some signals that had prominent near-DC frequency components.

These tests were done only using the stop-and-go mode, due to its easier processing, and allowed to develop an early version of the synthetic image formation code, which did not include any form of hardware acceleration. Most configuration was manual and error prone, fact that motivated incremental automation improvements, which made acquiring and processing data a much smoother process.

After extensive testing, the next step was to upgrade most parts of the system to include the multi-frequency capability. The rail and enclosures were upgraded to robust industrial grade units, and the integrated front-end assembly comprising all frequencies was designed and built. The next sections show the tests done with the upgraded system.

They are used in virtual machines. The emulation leads to reduced performance with respect to physical interfaces.

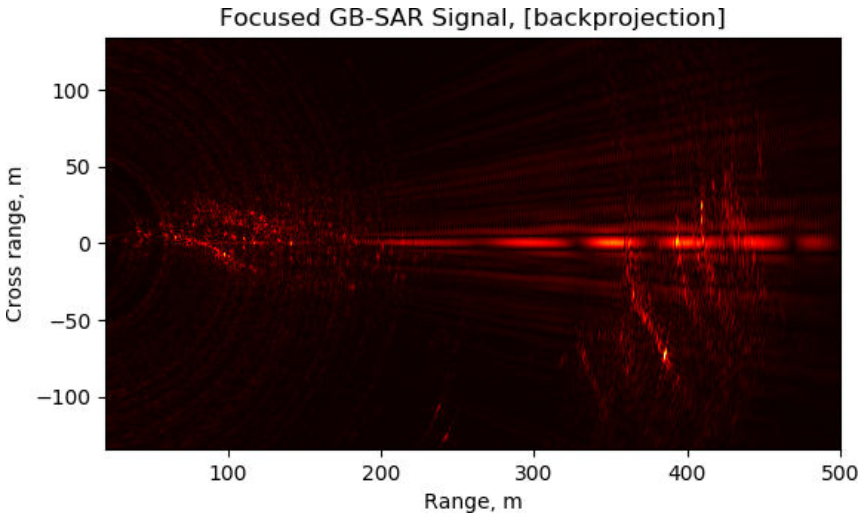

(a)

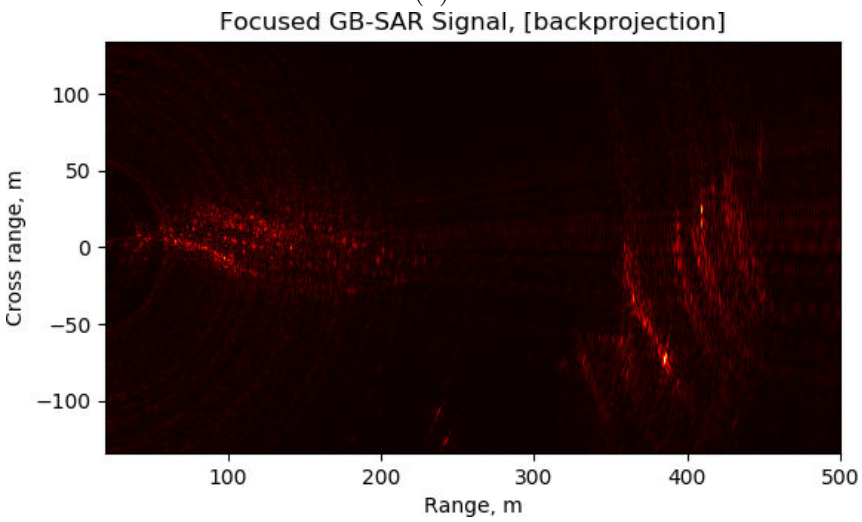

(b)

(c)

Figure 4.2: First SAR mode magnitude images. (a) Image with the zero azimuth spur due to IQ imbalance spurs. (b) Corrected image using the SSVA reconstruction algorithm. (c) Orthophoto of the first test site. Orthophoto credit: ICGC.

4.2 Muntanya Rodona field test site

The Muntanya Rodona test site is located in Subirats (Spain), south of Barcelona. It was chosen for its proximity to the radar storage, its easy accessibility and the presence of man-made targets such as buildings and other urban structures, which allowed for a fast assessment of correct synthetic image formation. This test site was used on numerous occasions to perform simple tests of added features or fixes in the radar system, and to get real-world feedback for a fast and agile design cycle. Although this design cycle consisted on many iterations through the duration of the thesis, they are not described in this document, and only the most relevant aspects are outlined. The results presented here represent the two last iterations performed on this site.

The main objective pursued in this test campaign was to reach a system maturity point that ensured its robust operation in future campaigns. This objective can be divided in smaller milestones:

- To ensure the reliable operation of the RF front-end, SDR and the linear unit.
- To automate most software procedures and system configuration, while ensuring the reliability of the software.
- To test the fast acquisition mode.
- To perform a qualitative assessment of the characteristics of measurements done at all frequencies.

In all the cases, the radar was located at 41°22'41.6"N 1°49'00.7"E, looking at the urbanization as shown in Figure 4.3b. The urbanization is on top of a small hill, with a maximum approximate elevation of 36 m with respect to the radar location as can be seen in Figure 4.3a. The targets imaged lie within a range 100 m to 200 m. The scene can be seen from the radar point of view in Figure 4.3c. A small corner reflector was placed at 100 m range, approximately. Although stop-and-go and fast acquisitions were made in the first measurements, all results presented from now on are taken using the fast mode. The reason for this, is that once the fast mode processing was operational, the stop-and-go mode was deemed inferior in all aspects, being the acquisition time the worst one in practical terms.

The logarithmic power Single Look Complex (SLC) images can be seen in Figure 4.4. From these, a qualitative assessment can be done about the characteristics of each band. The first effect to note is the evident loss of resolution, which worsens progressively as the frequency decreases. At X- and C-bands, the resolution is high enough to be able

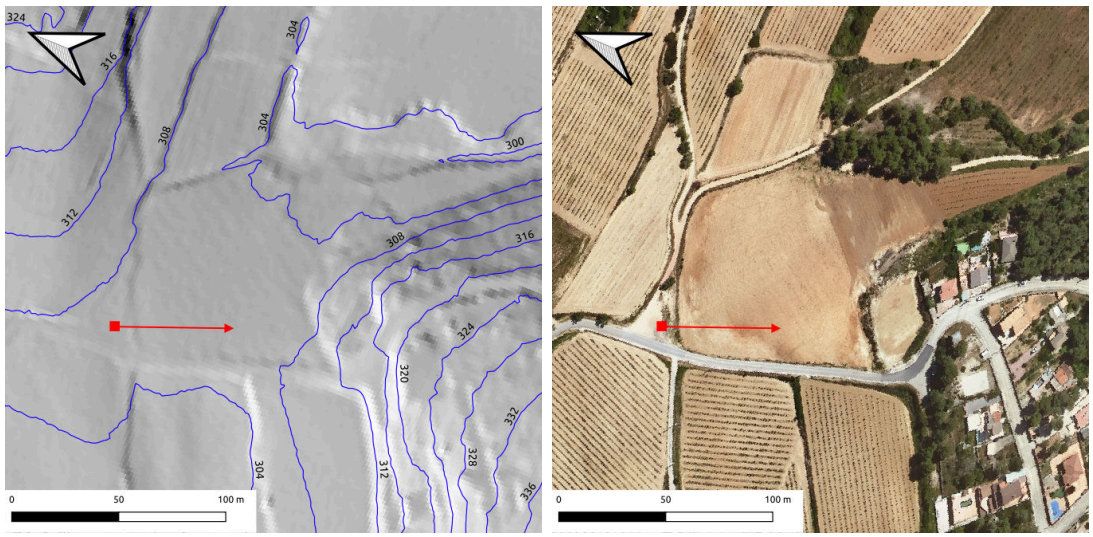

(a) (b)

(c)

Figure 4.3: Muntanya Rodona test area maps. (a) Elevation map. (b) Orthophoto. (c) Muntanya Rodona test area view from the radar position. The red square and arrow specify the radar location and azimuth look direction. Orthophoto and DEM credit: ICGC.

to correlate the orthophoto from Figure 4.3b with the radar images, being the buildings and the staggered geometry of the terrain the most distinctive features. At L-band, this correlation is more difficult to observe, while at P-band the shape of the scene is lost. The second effect to note is the progressive broadening of the illuminated scene, consistent with the broadening of the antenna beam patterns shown in Figure **??** and **??**. Another relevant aspect is the superior vegetation penetration characteristics at L- and P-band, as it can be seen, for example, at coordinates (170,-70). Also, a noticeable aspect is the dimming of the reflector as the frequency decreases, an effect of the decrease of the reflector RCS, combined with its smaller contribution within a bigger pixel.

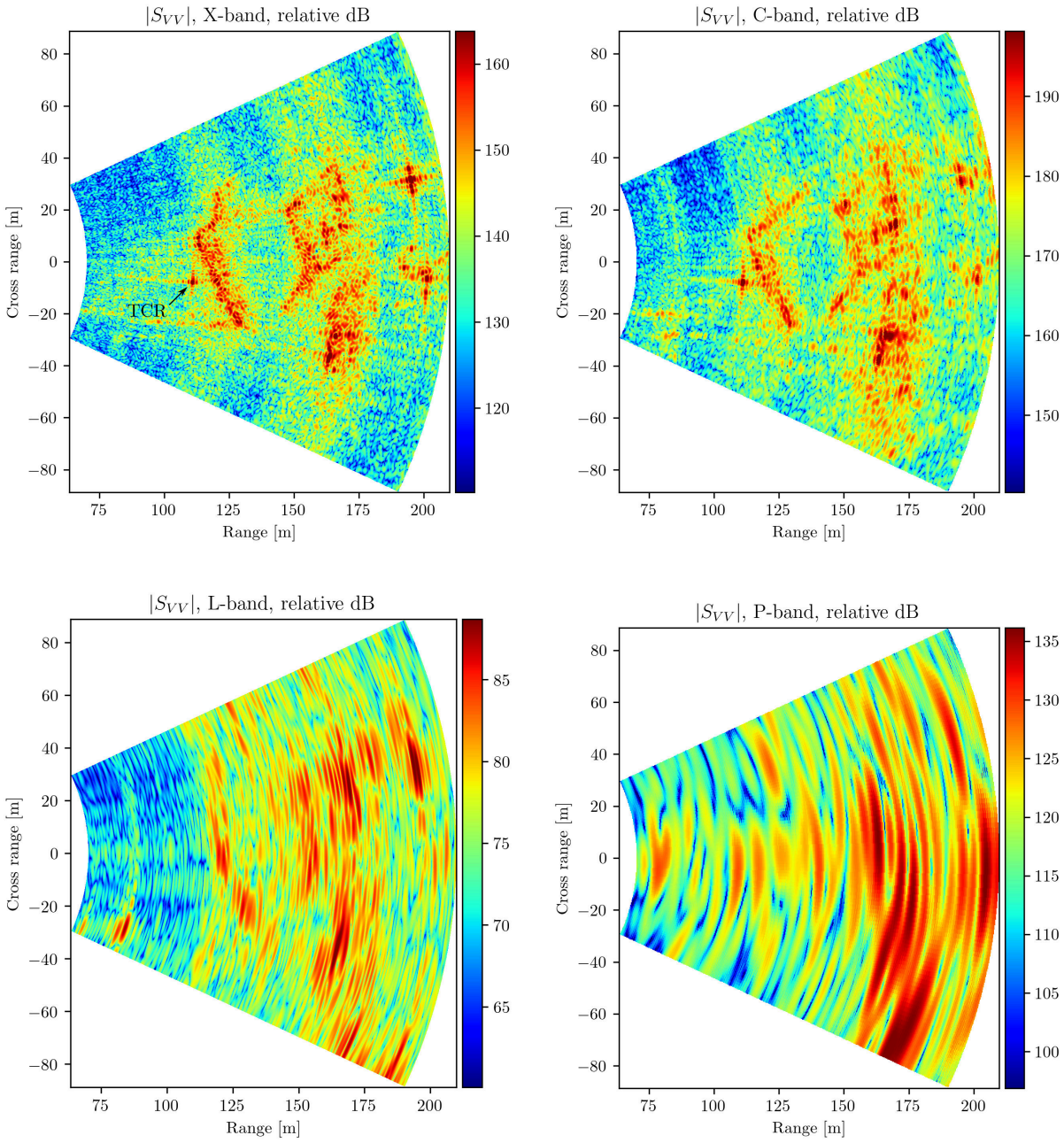

Figure 4.4: SLC power in decibels at all four frequencies. The absolute power is uncalibrated.

4.3 Subirats castle field test

The second batch of tests were done in the Subirats castle (Subirats, Spain), south Barcelona. These tests were aimed at performing more advanced tests that consisted on the generation of multi-frequency time series and the imaging of two big areas. The time series was used to exploit the temporal dimension and to observe the differences between frequencies, and to make an evaluation of the stability of the targets present in the scene. Regarding the other two areas, only a few images were taken, and served, mainly, to certify the capabilities of the radar to image far ranges and to generate coherence maps.

4.3.1 Test site nº 1

The first test site is a small area facing South from the castle. The radar was located at 41°24'57.9"N 1°48'59.2"E, at 289 m above sea level, with a depression angle of 10°, directly looking at the road shown in Figure 4.5a. The area consists on two vegetated hills separated by the road. The upper hill is vegetated mainly by mid-dense shrubland, with sparse rocky patches without vegetation, while the lower hill is more densely vegetated with a combination of shrubland and evergreen oaks. The difference in vegetation density is due to a wildfire that took place in 1994, which severely burnt the upper hill.

The location and scene was chosen due to its geometry, which is adequate to recreate the incidence angles typical of satellite SAR systems. Figure 4.5 shows an orthophoto and the elevation map of the area, and Figure 4.6 shows the scene from the point of view of the radar platform. Two TCRs were placed as external calibrators as shown in Figure 4.5a and 4.6. The first TCR had a 60 cm side, while the second one had a 30 cm one. In order to assist in the comprehension of the geometry of the area, Figure 4.7 provides a cross section of the DEM, cut along the plane consisting on the radar line of sight and nadir lines, and its corresponding slope profile.

The main objective of the first test site was to acquire long time-series along several hours in all frequencies in order. Specifically, the objectives were:

- To implement an accelerated focusing algorithm, as explained in Section **??**.
- To quantify to and certify the range and azimuth resolution.
- To examine the stability of the system.
- To test internal and external calibration procedures.
- To measure the temporal interferometric zero-baseline coherence of various areas including vegetation.

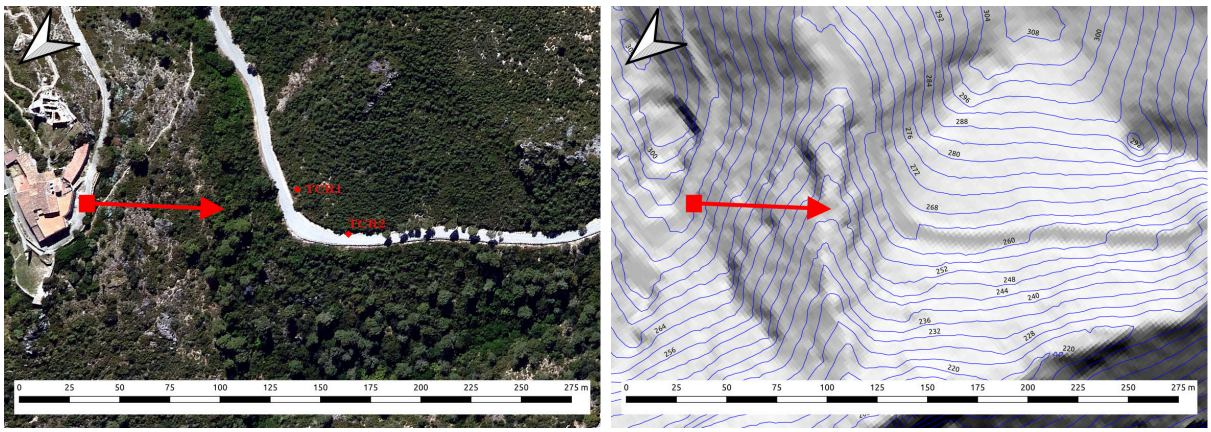

(a) (b)

Figure 4.5: Subirats castle test site nº1 orthophoto and elevation profile. The square and arrow indicate the radar position and azimuth view direction. The two TCR positions are also shown. Orthophoto and DEM credit: ICGC.

- To observe the enhanced penetration capabilities of L- and P-band.
- To assess the magnitude and phase stability of different areas along the acquisitions.

(a) (b) (c)

Figure 4.6: (a) Test site nº1 from the radar point of view. (b) TCR 1. (c) TCR 2.

The test consisted in acquiring a relatively long time-series at all frequencies. Every 8 minutes, approximately, a single acquisition (or frame) was done for each frequency, one after another without time gaps. For reference, Table 4.1 shows the acquisition times as well as the frequency bands used.

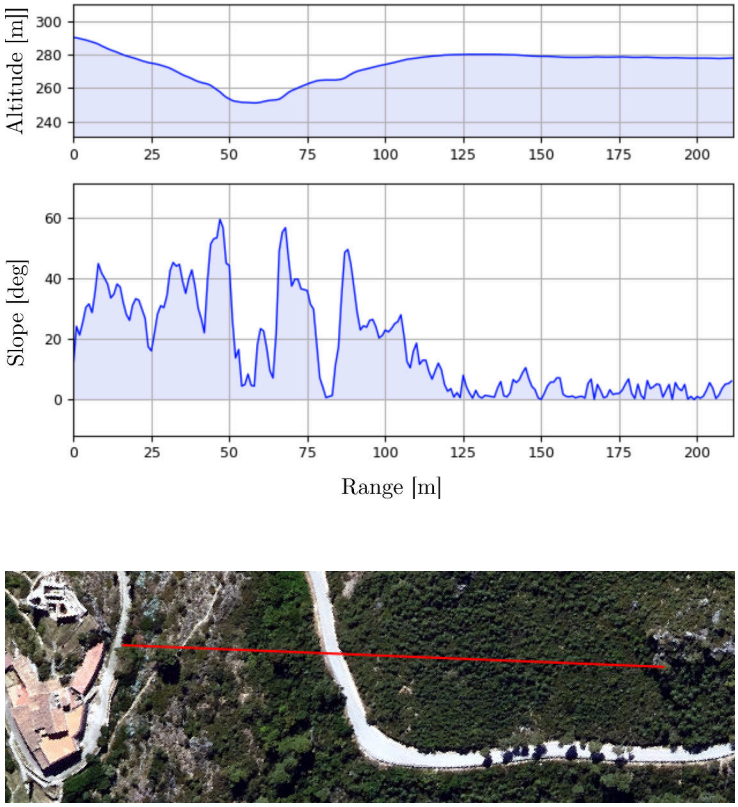

Figure 4.7: Height and slope profiles for the line path shown. The horizontal axis represents range. All dimensions are in meters. Orthophoto and DEM credit: ICGC.

Table 4.1: Acquisition times. Time format: HHMMSS.

Time	Band	Frame	Time	Band	Frame	Time	Band	Frame	Time	Band	Frame
131748	X	1	140819	L	6	144611	L	11	154514	X	17
131946	C	1	141018	P	4	144845	P	9	154656	C	17
132110	L	1	141254	X	7	145704	X	12	154821	L	16
132922	X	2	141357	C	7	145958	C	12	155115	P	14
133038	C	2	141502	L	7	151100	X	13	155309	X	18
133402	L	2	141910	P	5	151220	C	13	155418	C	18
134101	X	3	142104	X	8	151344	L	12	155534	L	17
134247	C	3	142222	C	8	151545	P	10	155805	P	15
134519	L	3	142331	L	8	151741	X	14	160002	X	19
134737	P	1	142533	P	6	151854	C	14	160108	C	19
135012	X	4	142724	X	9	151959	L	13	160224	L	18
135124	C	4	142838	C	9	152153	P	11	160849	P	16
135341	L	4	142942	L	9	152339	X	15	161049	X	20
135619	P	2	143454	P	7	152445	C	15	161157	C	20
135856	X	5	143739	X	10	152548	L	14	161308	L	19
140013	C	5	143848	C	10	152815	P	12	161516	P	17
140115	L	5	143950	L	10	153050	X	16	161705	X	21
140348	P	3	144154	P	8	153154	C	16	161824	C	21
140603	X	6	144335	X	11	153257	L	15	161928	L	20
140712	C	6	144455	C	11	153512	P	13	162140	P	18

The first image taken at each frequency can be seen in Figure 4.8. At X- and C-band, the two TCRs are strong and clearly visible, while at L- and P-bands their presence is less

evident, mainly because the secondary lobes of the PSF are buried under the surrounding distributed target energy. The road is clearly distinguishable at X- and C-band, as the rocky slopes and the metal guard rails at its edges are relatively strong reflectors. The broadening of the antenna beam is also evident as frequency lowers. This can be clearly observed at the upper edge of the X- and C- images: while the road shape is clear at C-band, at X-band the road and its surroundings are buried below noise. In order to aid in the visual correlation between the orthophoto shown in Figure 4.5 and the SLC images, a composite image between X-band and the orthophoto is shown in Figure 4.9. The X-band image is thresholded so that only the strongest pixels are shown.

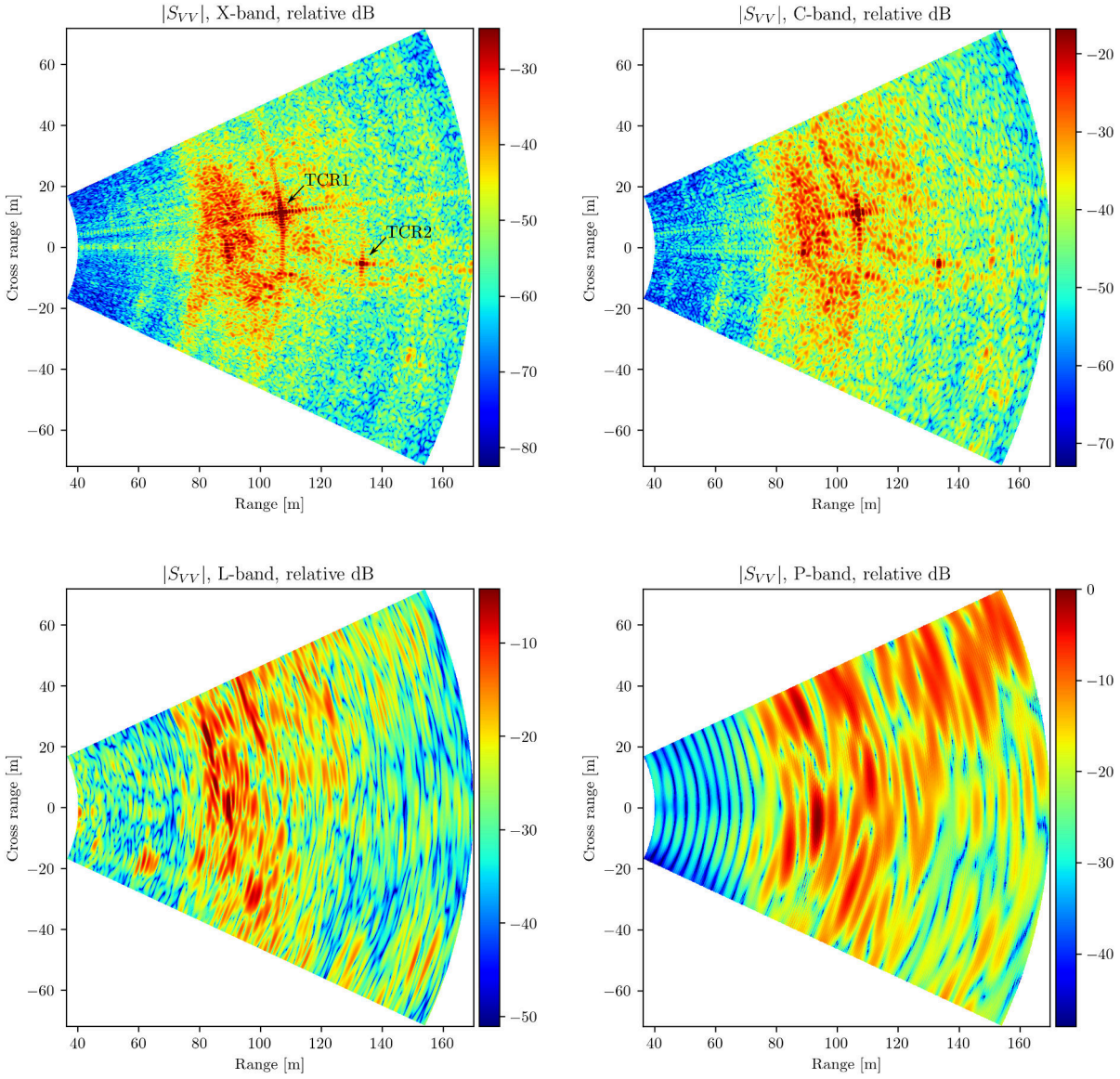

Figure 4.8: SLC images at all frequencies. The absolute power is uncalibrated.

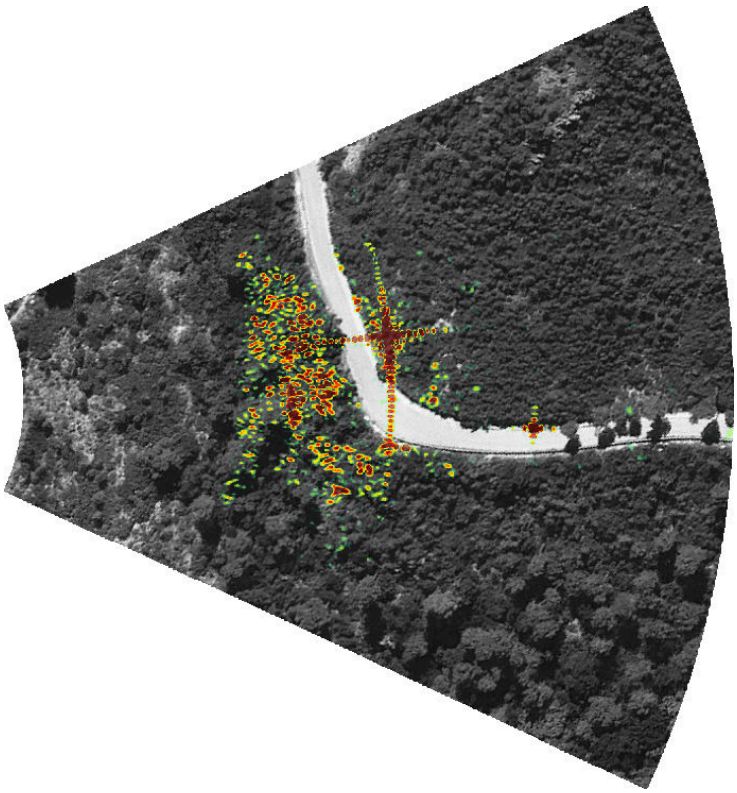

Figure 4.9: Composition of the orthophoto and the thresholded magnitude X-band image. Orthophoto credit: ICGC.

These images are also used to quantify and certify the range and azimuth resolution. The quantification is done here due to the usage of a bigger reflector (TCR1) than in the previous test campaigns. In order to do so, TCR range and azimuth cuts are extracted from the polar format data for X-, C- and L-band, and the 3 dB width of the main lobe is examined. The cuts are shown in Figure 4.10. The measured range resolutions are 0.9 m for all three bands, as the signal bandwidth is the same for all, and the measured azimuth ones are 7 mrad, 13 mrad and 66 mrad [2], for X-, C- and L- bands, respectively. This is in perfect agreement with the theoretical values specified in Table **??**. The values at P-band are not shown since the TCR signal to clutter ratio is not high enough to yield reliable values.

[2]Note that the resolution in milliradians is equivalent to the resolution in meters at a range of 1 km

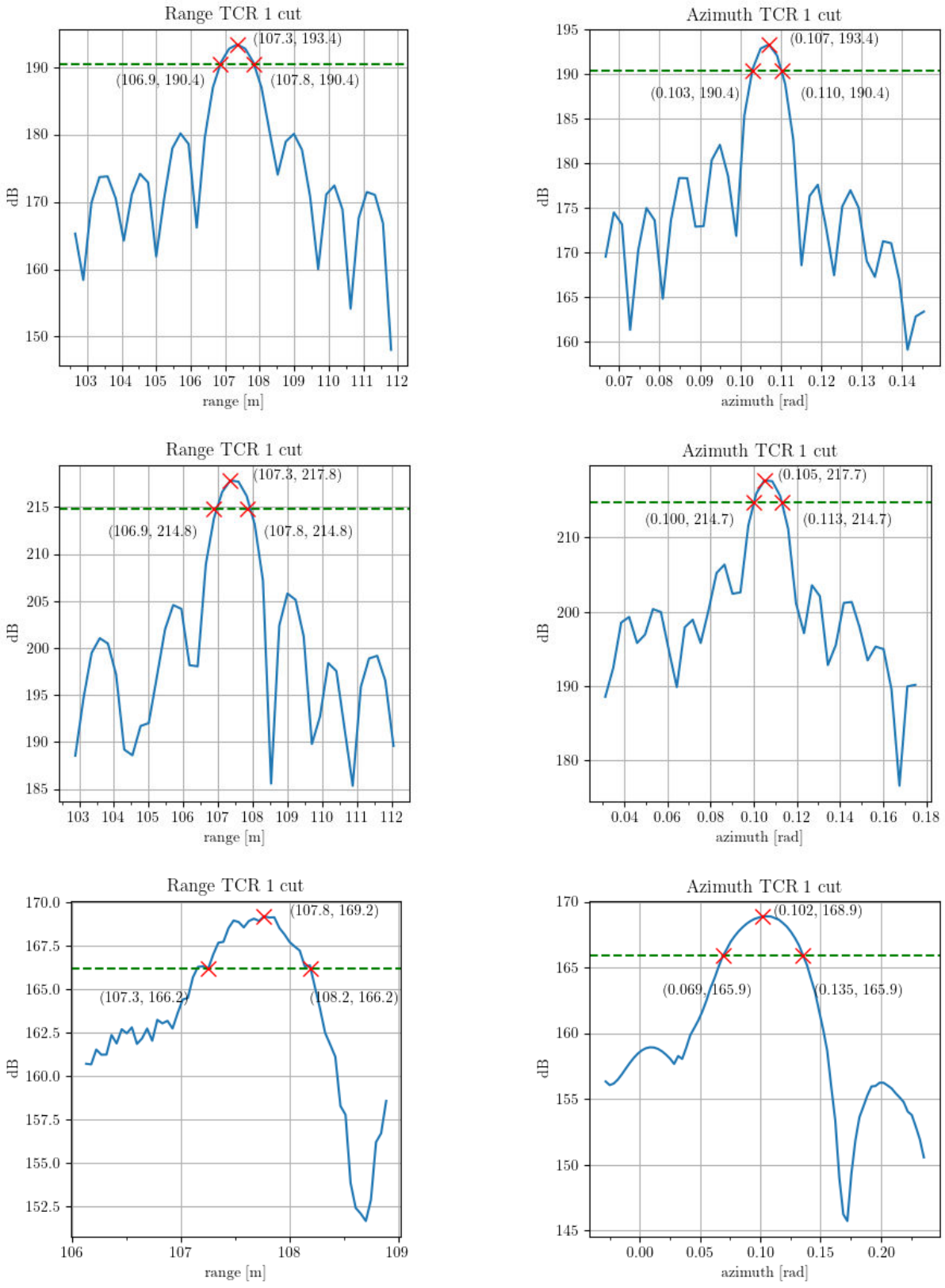

Figure 4.10: TCR cuts. From top to bottom: X-band, C-band and L-band. Note that the absolute magnitude values are not calibrated.

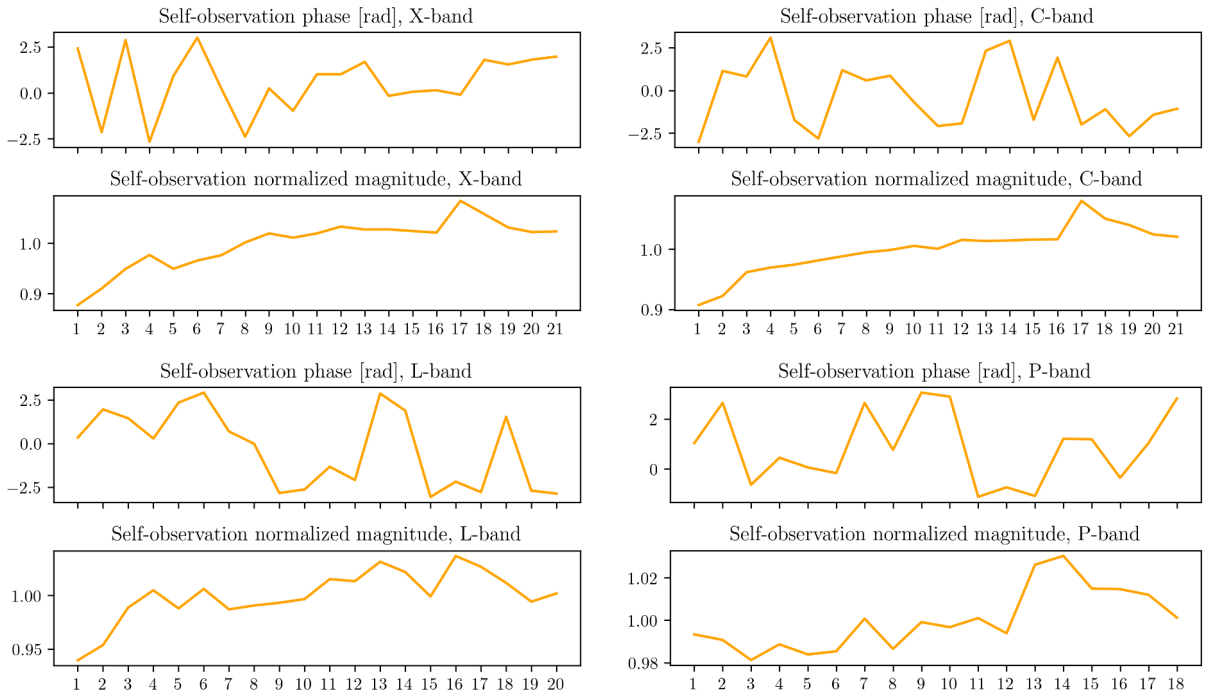

Figure 4.11: Magnitude and phase stability vs. acquisition number for all bands versus acquisition number.

Examining the system stability is another objective of this campaign. This is accomplished by extracting the phase and magnitude of the observation signal saved at the beginning of each acquisition. The phase and magnitude extracted from each acquisition can be seen in Figure 4.11. As expected, the observed phase is random due to PLL relocks, as stated in Section **??**. The magnitude at X- and C- bands exhibit an exponential profile, converging to a stable value, while at L- and P- bands this exponential shape is not clearly observed. This increase in magnitude is due to change in the overall system gain as temperature increases. This increase is a rather unexpected result, as the gain in most RF devices drops as temperature increases, and further investigation is needed in this aspect. These changes are not critical, since they are calibrated before the focusing process.

After internal phase and magnitude compensation, the reflectors can be observed. Assuming they are stable targets, they should ideally present a fixed phase and magnitude. Observing the corner reflectors or other strong, stable targets can be useful in making assessments of atmospheric effects and aid in their eventual correction [82]. The magnitude and phase of the TCRs are shown in Figure 4.13, Figure 4.14, Figure 4.15 and Figure 4.16. At X- and C- bands, the chosen reflectors are both TCRs, while at L- and P- bands only one reflector is used, and chosen to be a natural target consisting on a relatively big rock

undisturbed by vegetation, as shown in Figure 4.12. In this case, the choice of using a natural target instead of a TCR lead to a more stable phase and magnitude. This can be explained by realizing that the relative contribution of the TCR within its pixel strongly decreases with decreasing frequency, as its RCS decreases and the pixel size increases. This leads to an increased contribution of the vegetation and other clutter to the given pixel, leading to increased instability, while the natural rock target size is comparable to the pixel sizes at L- and P- bands.

Figure 4.12: Detail of the bare rock used as stable target.

A close observation of the reflector phases reveals that X-band suffers a slow phase instability, probably due to slowly changing atmospheric humidity and temperature, and the presence of some peaks, which are observed in both reflectors, fact that discards a hardware cause, and can be attributed to fast changes in atmospheric conditions. At C-band, TCR1 shows an enhanced stability, while TCR2 is more unstable as a result of its smaller size. At L- and P- bands, the natural reflector exhibit a similar stability than TCR1 at C-band.

Another analysis that can be done, and which represents an important point in this thesis, is analysing the magnitude and phase stability in the whole area by means of the phase standard deviation and amplitude (or magnitude) dispersion index, which is a measure of amplitude stability. The amplitude dispersion index is defined as [83]:

$$D_A = \frac{\sigma_A}{m_A}. \tag{4.1}$$

Where σ_A is the amplitude standard deviation and m_A is the amplitude mean value. Similarly, the phase stability σ_ν can be assessed with its standard deviation and can be shown to be $\sigma_\nu \simeq D_\mathcal{A}$ for high Signal to Noise Ratio (SNR) [83]. The dispersion amplitude is an important metric used in interferometric SAR and is an indication of stable targets

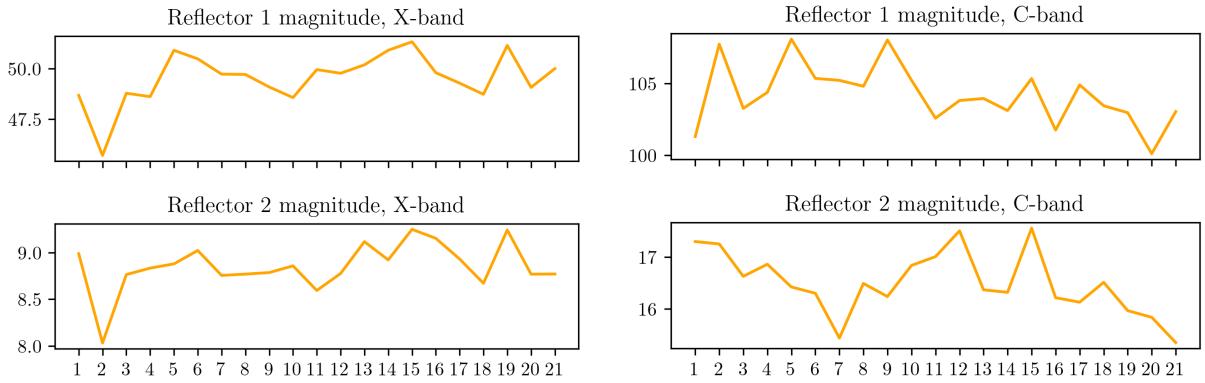

Figure 4.13: Relative magnitude of the two TCRs for X- and C- bands versus acquisition number.

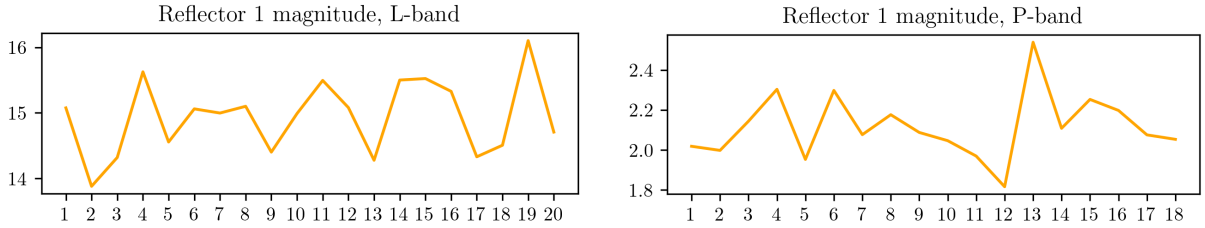

Figure 4.14: Relative magnitude of a strong and stable natural reflector for L- and P-bands versus acquisition number.

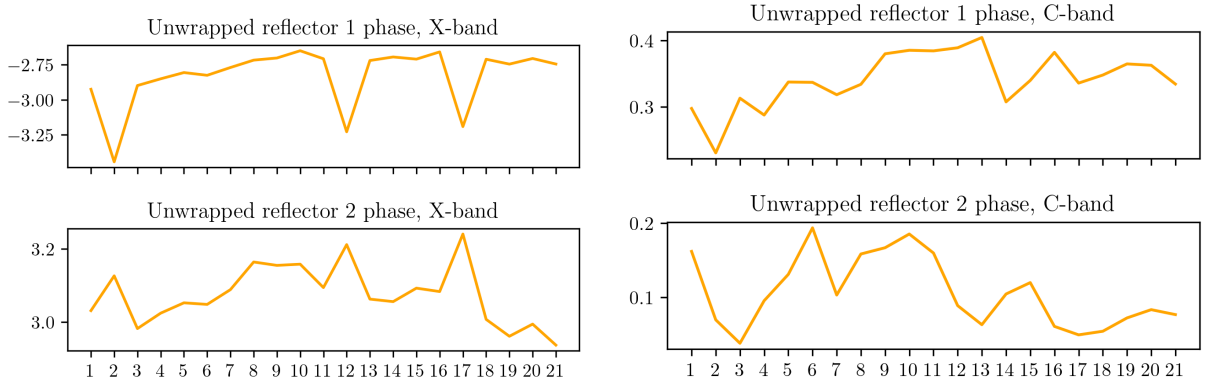

Figure 4.15: Phase of the two TCRs for X- and C- bands versus acquisition number.

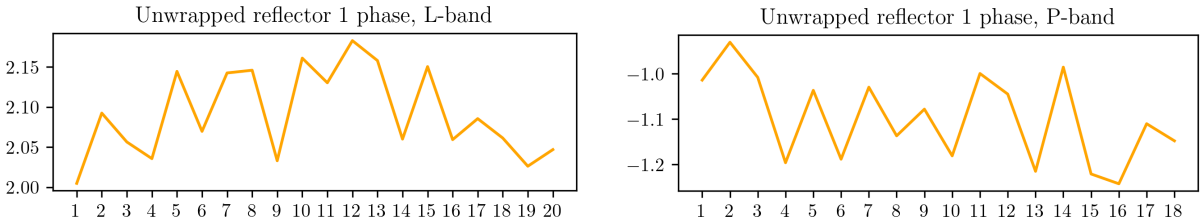

Figure 4.16: Phase of a strong and stable natural reflector for L- and P-bands versus acquisition number.

or areas that can be exploited. Maps of both metrics are shown in Figure 4.17 and 4.18. It can be observed in both figures that at X- and C- bands the most stable targets are the two TCRs, the edges of the road and occasional points in the vegetated areas. From the last ones, there is a cluster at (90,0) m that is identified as a big, bare rock in direct view from the radar used as a calibrator for L- and P-bands. Comparing the X- and C-band stability maps, it can be seen that the C-band map contains more dense clusters of stable points, for instance at around (95,-20)m, indicating the higher X-band sensitivity to foliage. At L-band, a drastic increase in stability occurs, and the presence of relatively stable points is evident in areas where X- and C-band show almost complete decorrelation. Note, for instance, that in the L-band phase image of Figure 4.17, a strong and very stable target appears at (80,20)m. At P-band, the stability improvement becomes stronger, and stable points are widespread in the imaged area. The normalized amplitude and phase stability of this target can be seen in Figure 4.19. Note the large difference in amplitude and phase stability between the X- and C- bands and the L- and P- bands. This is a clear indication of stable target detection below vegetation.

Taking the magnitude dispersion index map, the Persistent Scatterers (PSs) present in the area can be identified. PS are strong, coherent targets that remain coherent over all acquisitions, and which are important in applications such as InSAR and aid in atmospheric effects compensation [82, 83]. The PS are extracted from the amplitude dispersion index image, which is almost insensitive to atmospheric effects [82], by selecting points with a given threshold, typically $D_A \leq 0.15$. Maps of the selected PS are shown in 4.20.

These results evidence the capability of the system to extract useful information from stable targets located under vegetation using L- and P-band. As a matter of speculation, a proper fusion of the data from different bands could lead to interesting applications where the benefits of each band are exploited. Another quantitative aspect that can be evaluated is the interferometric coherence. Coherence can be defined as [84]:

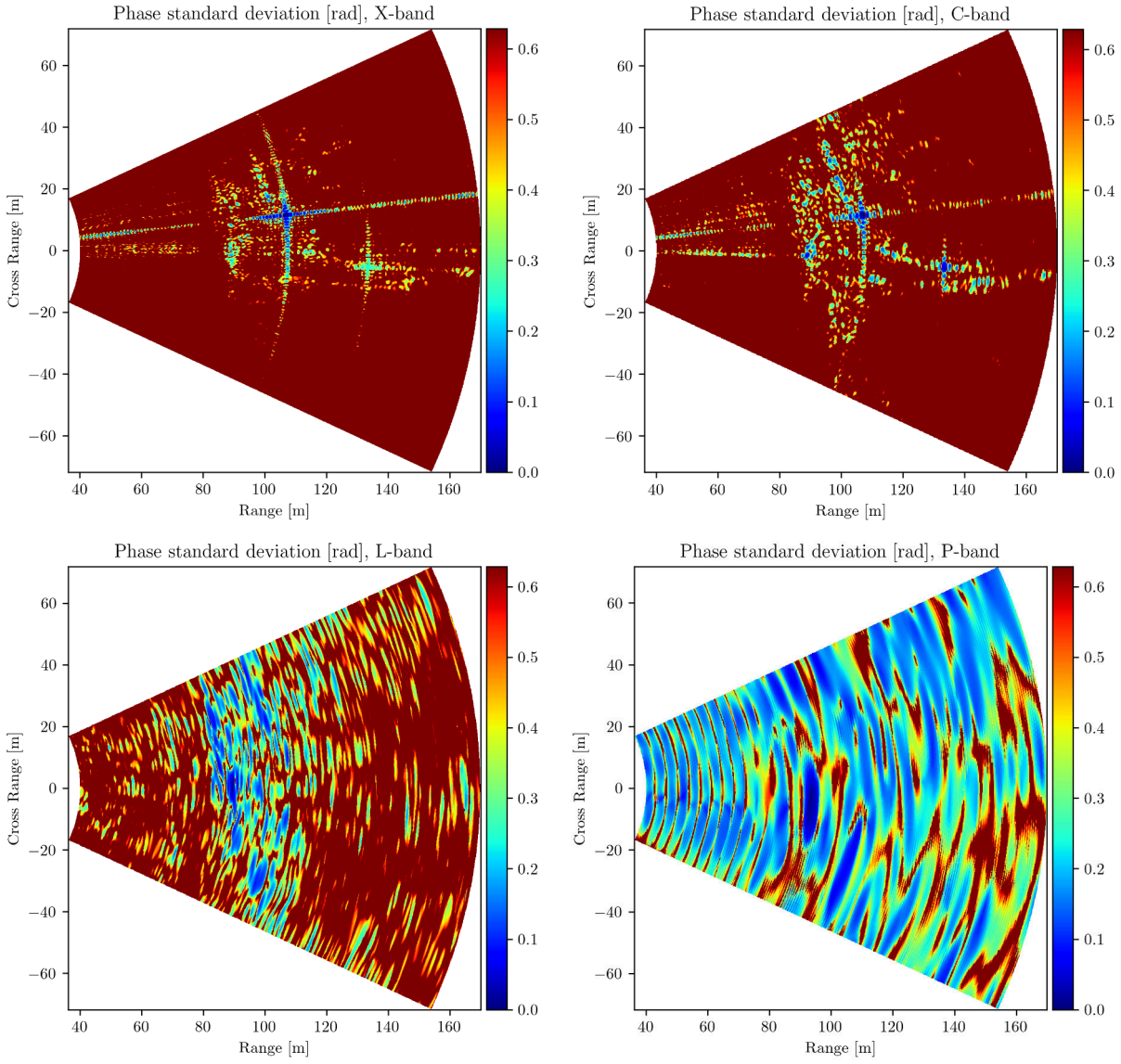

Figure 4.17: Phase standard deviation maps. The values are clipped at $\pi/5$.

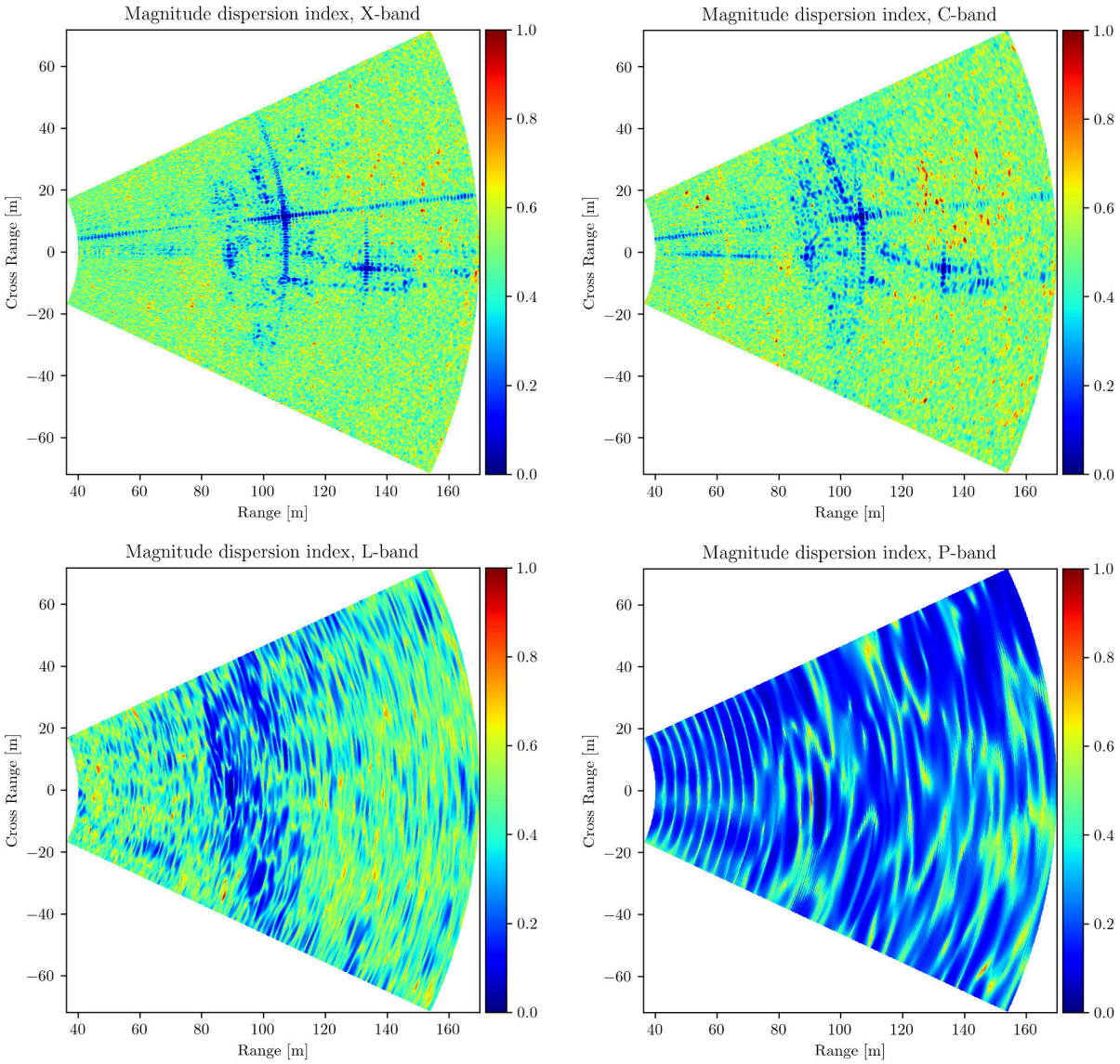

Figure 4.18: Magnitude relative standard deviation maps.

$$D = \left| \frac{E\left(z_1 z_2^*\right)}{\sqrt{E\left(|z_1|^2\right)}\sqrt{E\left(|z_2|^2\right)}} \right|. \tag{4.2}$$

Where E is the expectation operator and z_1 and z_2 are two zero-mean complex signals for wide-sense stationary processes. In order to estimate D, it is assumed that the random process is ergodic in mean, and the sample coherence estimator is defined as

Figure 4.19: Amplitude and phase stability of the rocky area under vegetation.

$$\delta = \left| \frac{\sum_{i=1}^{N} z_{1i} z_{2i}^{*}}{\sqrt{\sum_{i=1}^{N} |z_{1i}|^2} \sqrt{\sum_{i=1}^{N} |z_{2i}|^2}} \right|, \tag{4.3}$$

where N is the number of signal measurements, which are ideally independent, and can represent a set of given pixels from a given pair of SLC images.

Coherence has a widespread use in many applications, such as in target classification [85] or in the generation of interferometric products such as DEMs or displacement maps [84]. Specifically, in the case of ground-based acquisitions, coherence can be exploited for the selection of PS points [86]. Its advantage lies in the reduced set of images required to determine the stable areas, and its disadvantage is a reduced set of coherent points due to the inherent loss of resolution of coherence estimation.

It can be demonstrated that the sampled coherence estimator is biased, especially for

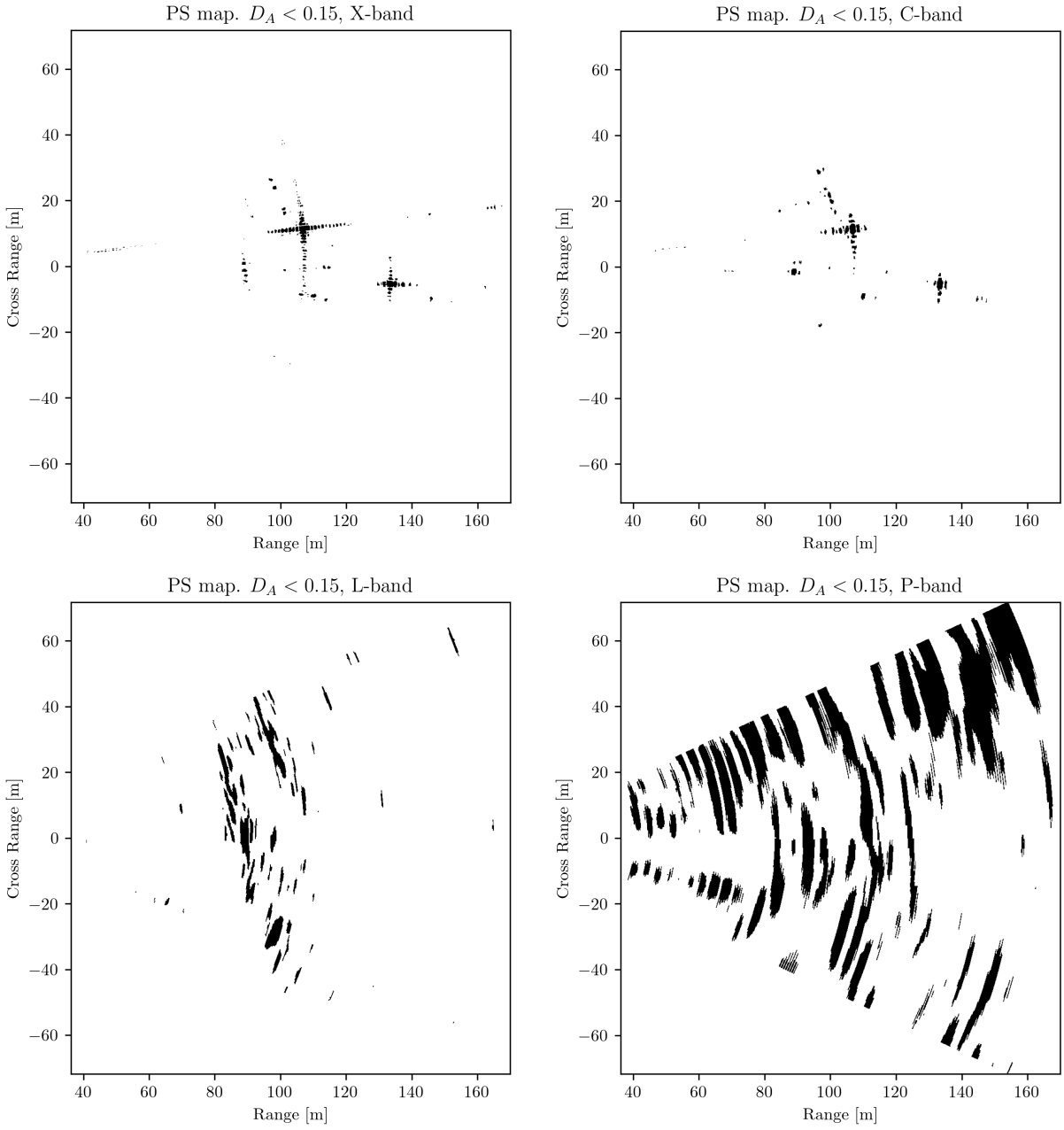

Figure 4.20: Persistent scatterer maps for each frequency.

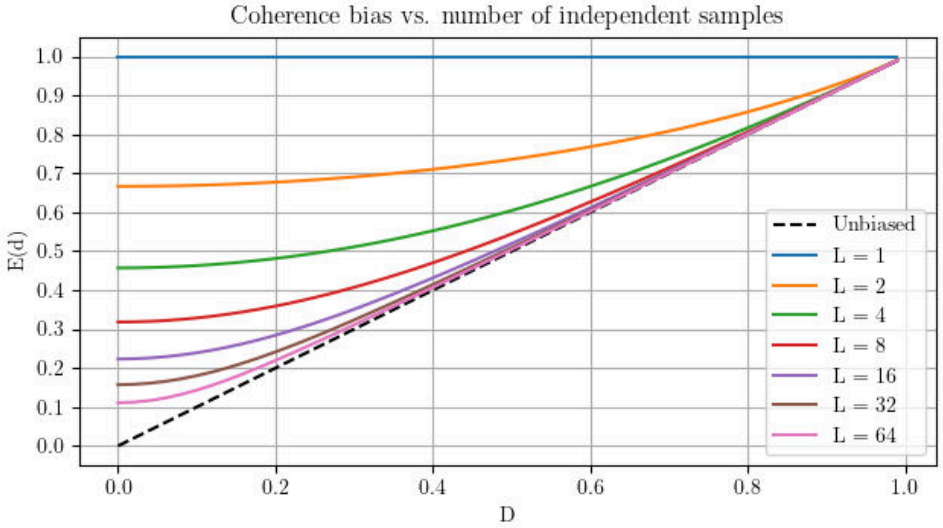

Figure 4.21: Coherence bias versus independent number of samples.

low coherence values [84]. The expectation of the sampled coherence is:

$$E(d) = \frac{\Gamma(L)\Gamma(1+1/2)}{\Gamma(L+1/2)} \times {}_3F_2\left(3/2, L, L; L+1/2; 1; D^2\right) \times \left(1-D^2\right)^L. \tag{4.4}$$

Where L is the number of independent samples, Γ is the gamma function and ${}_pF_q$ is the generalized hypergeometric function [87]. In Figure 4.22, the expectation of the sampled coherence is plotted against the real coherence and L. This indicates that, in order to perform a valid estimation, a sufficient number of independent pixels have to be used. The number of independent pixels is also referred as the Effective Number of Looks (ENL). In order for the coherence estimation to have sense, it is usually estimated taking a given set of pixels from uniform areas. Coherence is usually presented in form of coherence maps, which are generated by a sliding window that selects the pixels to be used. Bigger windows imply less estimation bias and variance, but imply coarser resolution maps.

In this case, as the imaged area is relatively small, instead of generating a coherence map, a single coherence value is estimated over entire areas representing different types of targets. For each area and for each frame, a value is computed. It has to be ensured that the ENL value is sufficiently high so that the estimate can be considered accurate. The areas chosen are depicted in Figure 4.23. The first area corresponds to the upper hill, comprising a range between 100 m and 130 m, just at the upper part of it. The second area is located at the same azimuth angle than the first one, but comprises a similarly vegetated area with flat terrain. Finally, the third area is a smaller area of the lower hill,

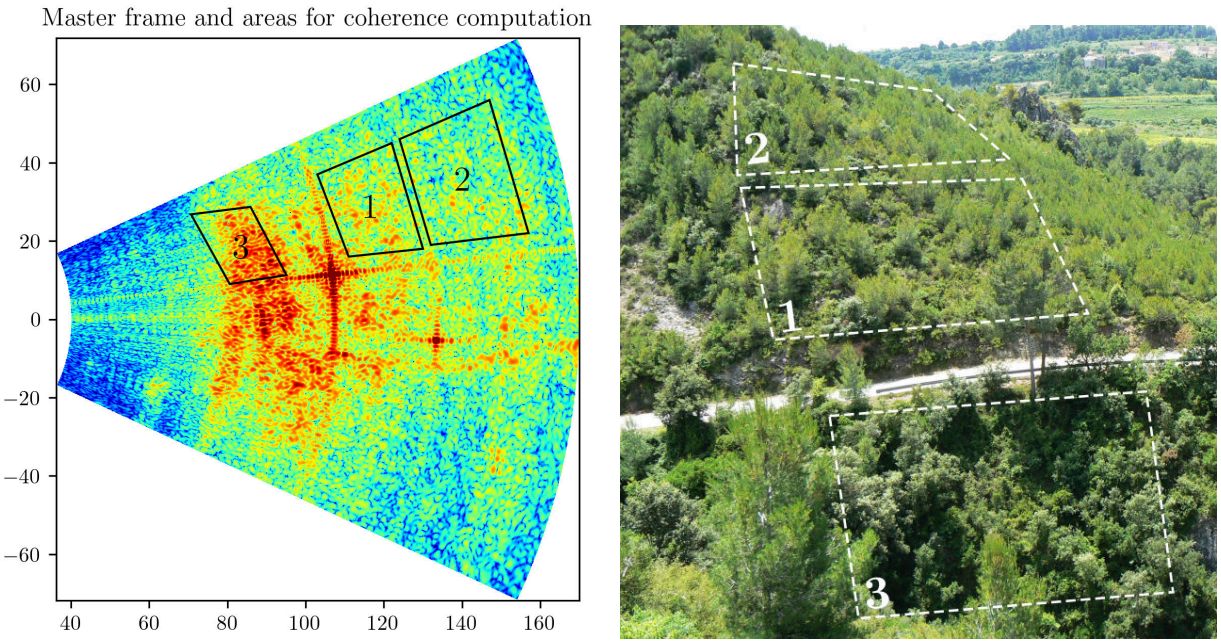

(a) (b)

Figure 4.22: Areas used for coherence computation shown over a reference X-band image.

with denser vegetation but containing various spots of very almost bare soil covered with a thin layer of vegetation. A rough approximation of the effective number of looks for each area and frequency is shown in Table 4.2. This table has been calculated by using the azimuth and range resolutions at each area, and dividing the resulting area of a pixel, which divides the extension of the area. This rough approximation could overestimate the ENL, as each resolution pixel is not entirely independent of the others due to the spread of the PSF [88]. For each case, it has to be judged whether a slight overestimation of the ENL could have a significant effect on the estimation. For a given coherence, the bias for the estimated ENL is examined, and the hypothetical ENL value that would produce the observed value is extracted from Figure 4.22. The difference between both values provides a way to judge whether the estimated value is biased or not.

The estimated coherence values of all three frames with respect to the first one, taken as the master frame, can be seen in Figure 4.24 for all four frequencies. Starting with X-band, the first thing to note is the differing values for all three areas. The high coherence of Area 3 can be explained by the very low density vegetation spots and the direct view of tree trunks, which are high coherence targets. The coherence of Area 1 is reduced due to the more consistent vegetation cover, while Area 2 presents a significantly lower coherence value. This low coherence value may be explained by the consistent and complete vegetation cover. At C-band, the coherence values are nearly identical, denoting a similar ability to

X-band to penetrate medium-dense vegetation. At L-band, a drastic coherence increase is observed at all three areas, which is expected due to the significant enhancement in penetration depth. Finally, at P-band, almost complete coherence is achieved at all three areas, proving the high insensitivity of this band to the type of vegetation present in the scene. Also, a slow decrease in coherence is clearly observed at X-band, and in a lower degree at C-band, which may correlate with slow changes in atmospheric conditions or changes in some terrain parameters such as soil moisture.

The coherence values of Figure 4.24 have to be examined along with the estimated ENLs to certify that they are good estimates. At X-band, the estimated ENLs are higher or equal than 490, which, from Table 4.2, imply biases much lower than the coherence values measured. In fact, from the lowest coherence estimated, an ENL > 64 suffices. The same reasoning applies for C-band. At L-band, for the lowest coherence measured to be biased, the ENL should be lower than about 3, much lower than the ENL estimates. The same applies to P-band, with coherence values very close to 1, an ENL > 2 would suffice, which is again significantly lower than the estimated ENL values.

In addition to the coherence graphs with respect to the master frame, Figure 4.26 shows the coherence matrices for all frequencies and areas. These matrices show the coherence of all frame combinations, and are a generalization of the coherences shown in Figure 4.24. In order to assist data interpretation, the same data is presented aggregated by area for all frequencies in Figure 4.25.

Table 4.2: Effective Number of Looks.

Frequency	**X**	**C**	**L**	**P**
Area 1	615	332	74	11
Area 2	811	438	97	15
Area 3	490	264	59	9

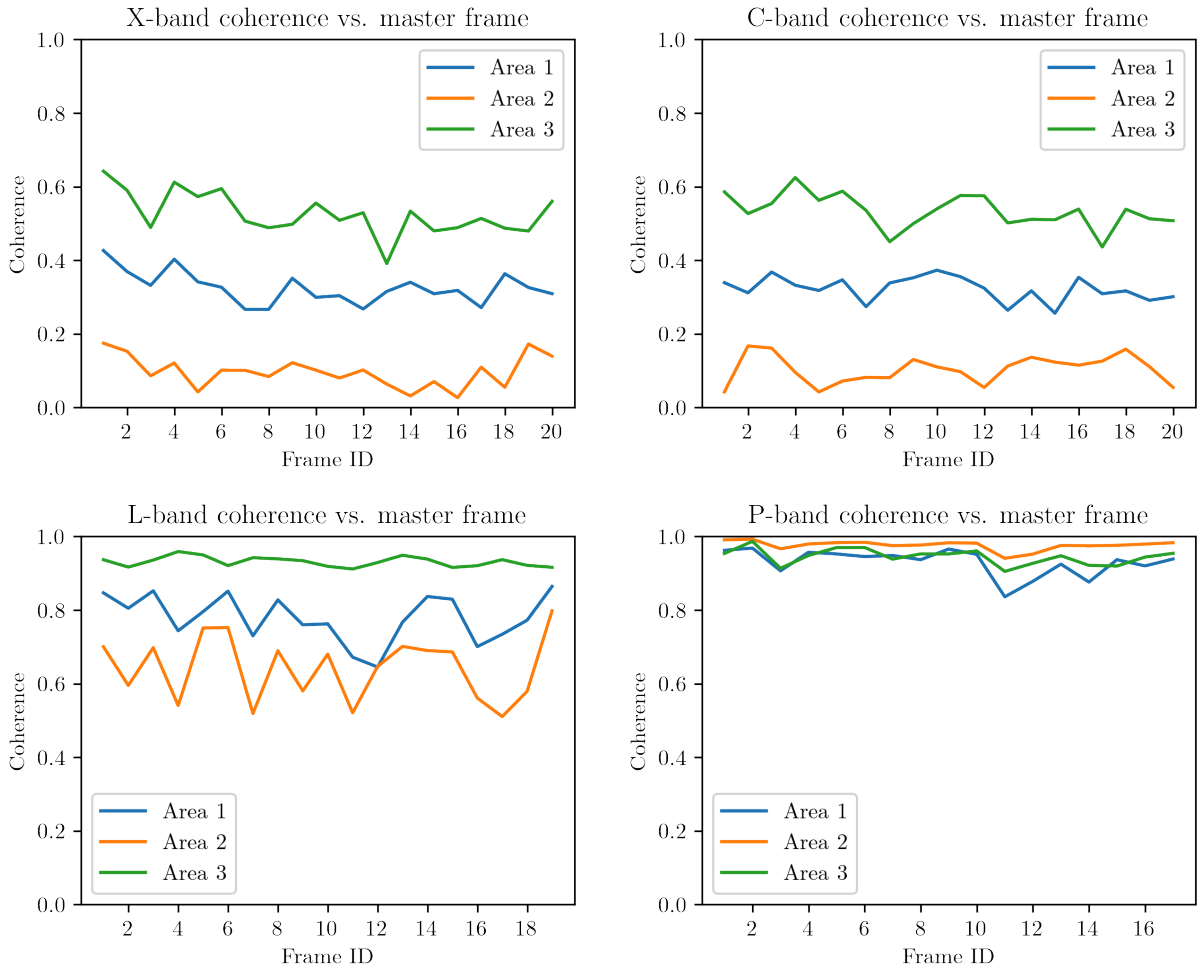

Figure 4.23: Coherence values of all frames with respect to the master frame, for all areas and frequency bands.

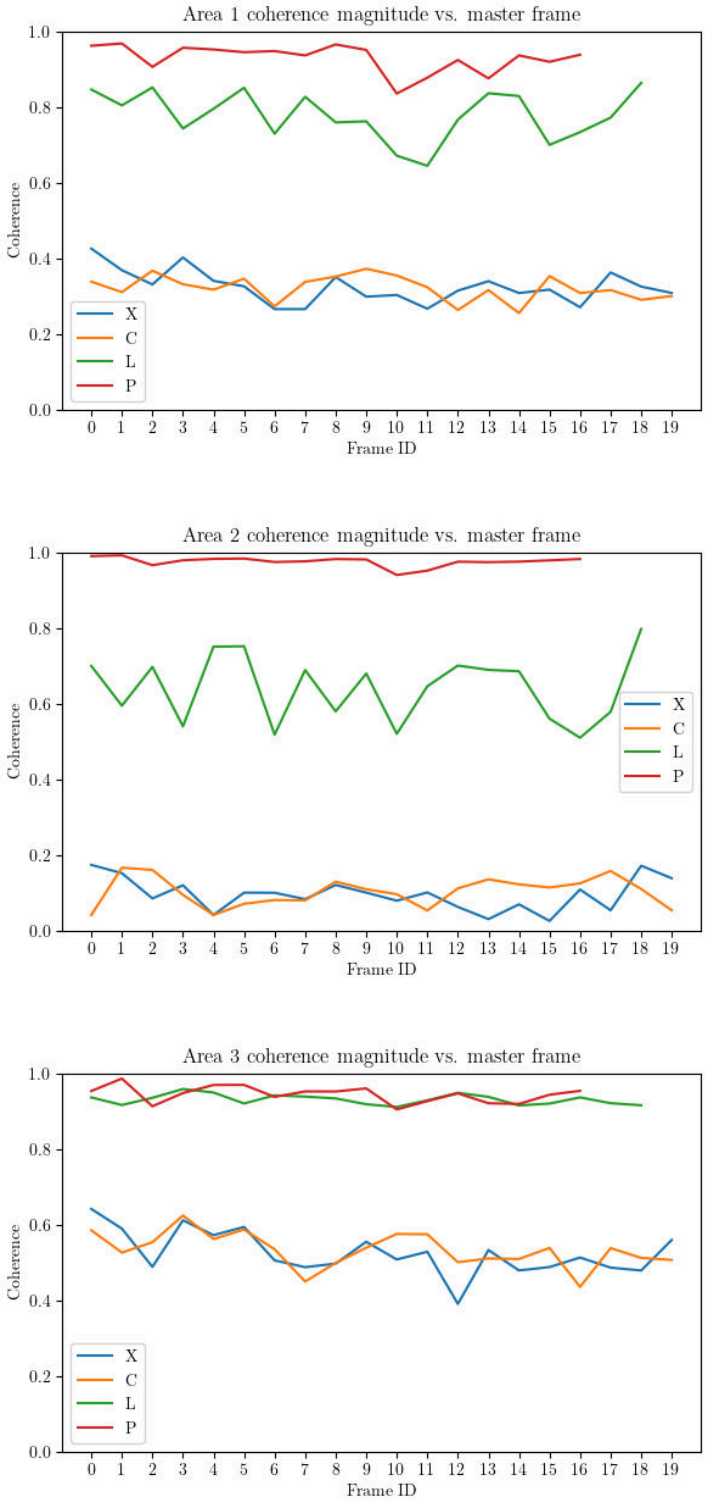

Figure 4.24: Coherence values of all frames with respect to the master frame, aggregated by area.

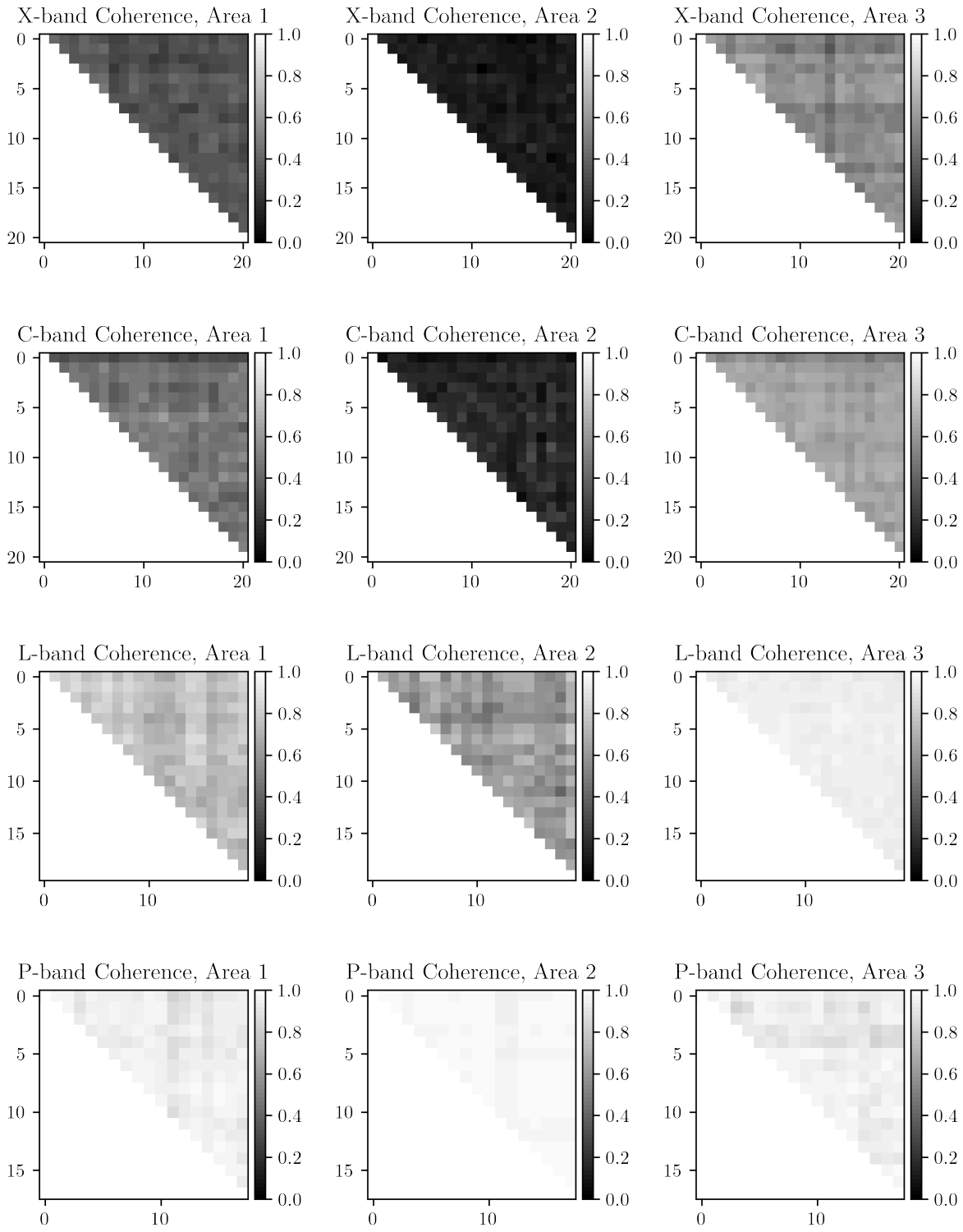

Figure 4.25: Coherence matrices for the three areas.

4.3.2 Test site nº 2

The second test site is set to image a farther range, while the radar is placed at exactly the same spot, except with a different pointing angle. An orthophoto and its corresponding elevation map are shown in Figure 4.27. The ranges imaged fall within 200 m to about 1200 m. The imaged scene consists mainly on dense vegetation, vineyards and some man-made structures such as low-rise houses and communication and electrical towers. An elevation and slope profile can be seen in Figure 4.29, which shows that the imaged area is mainly a smooth uphill from 600 m to 1200 m. Figure 4.28 shows the scene from the point of view of the radar platform, along with a zoomed image of the artificial structures.

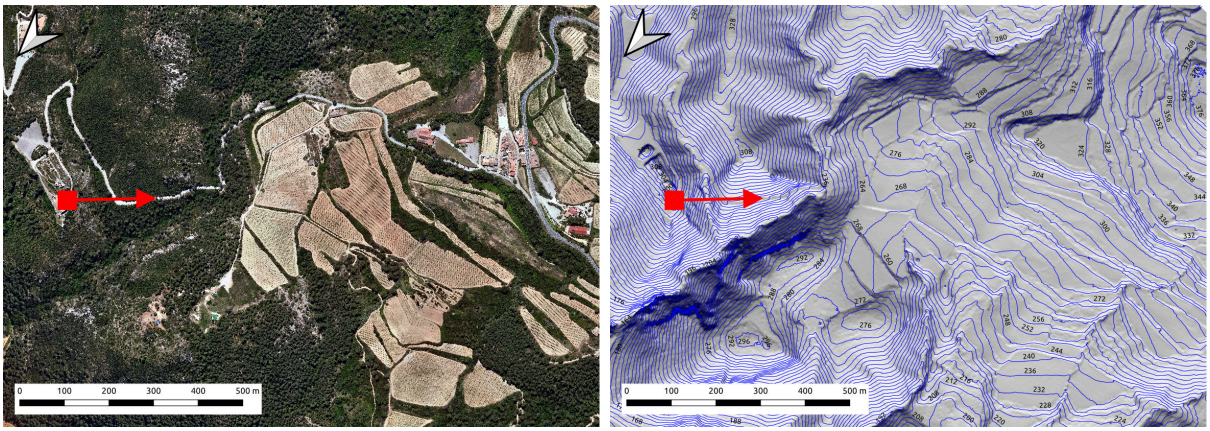

(a) (b)

Figure 4.26: Test site nº2 orthophoto and elevation profile. The square and arrow indicate the radar position and azimuth view direction. Orthophoto and DEM credit: ICGC.

The objective of this test is to certify that the system can image far targets, the generation of coherence maps and that the image formation algorithm can deal with large areas.

A sample of the SLC images at each band can be shown in Figure 4.30. In order to aid in its interpretation, a composite of the thresholded X-band magnitude image and an orthophoto is provided in Figure 4.31.

These images showed, unexpectedly, the presence of a spurious signal at zero azimuth, similar in form to the one shown in Figure 4.2a. After a short investigation period, it was determined that the spur was caused by the leakage of the 10 MHz reference clock to the RF signal paths. The reference clock is up- and down-mixed at different stages of the external front-end, leading to a similar mechanism than the one explained in Section **??** for the effects of the in-phase and quadrature (IQ) imbalance spurs. The reference clock harmonics are seen as chirp-like signals at the reception (RX) channels, resulting

(a)

(b)

Figure 4.27: (a) Test site nº2 from the radar point of view. (b) Detail.

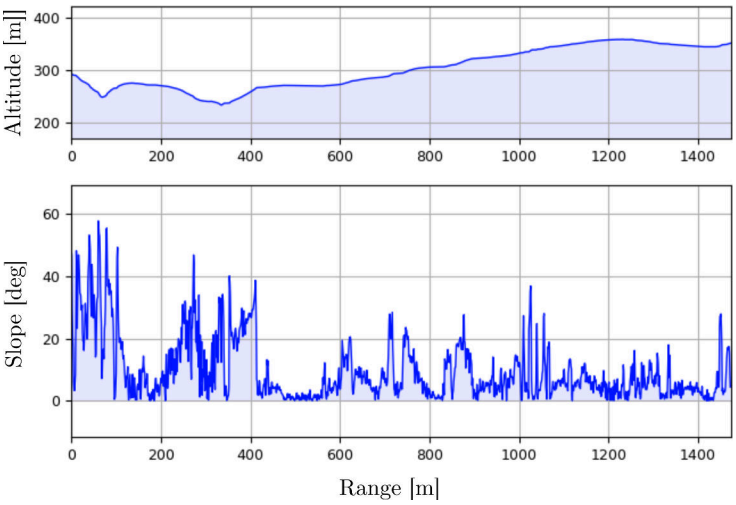

Figure 4.28: Height and slope profiles for the line path shown. The horizontal axis represents range. All dimensions are in meters. Orthophoto and DEM credit: ICGC.

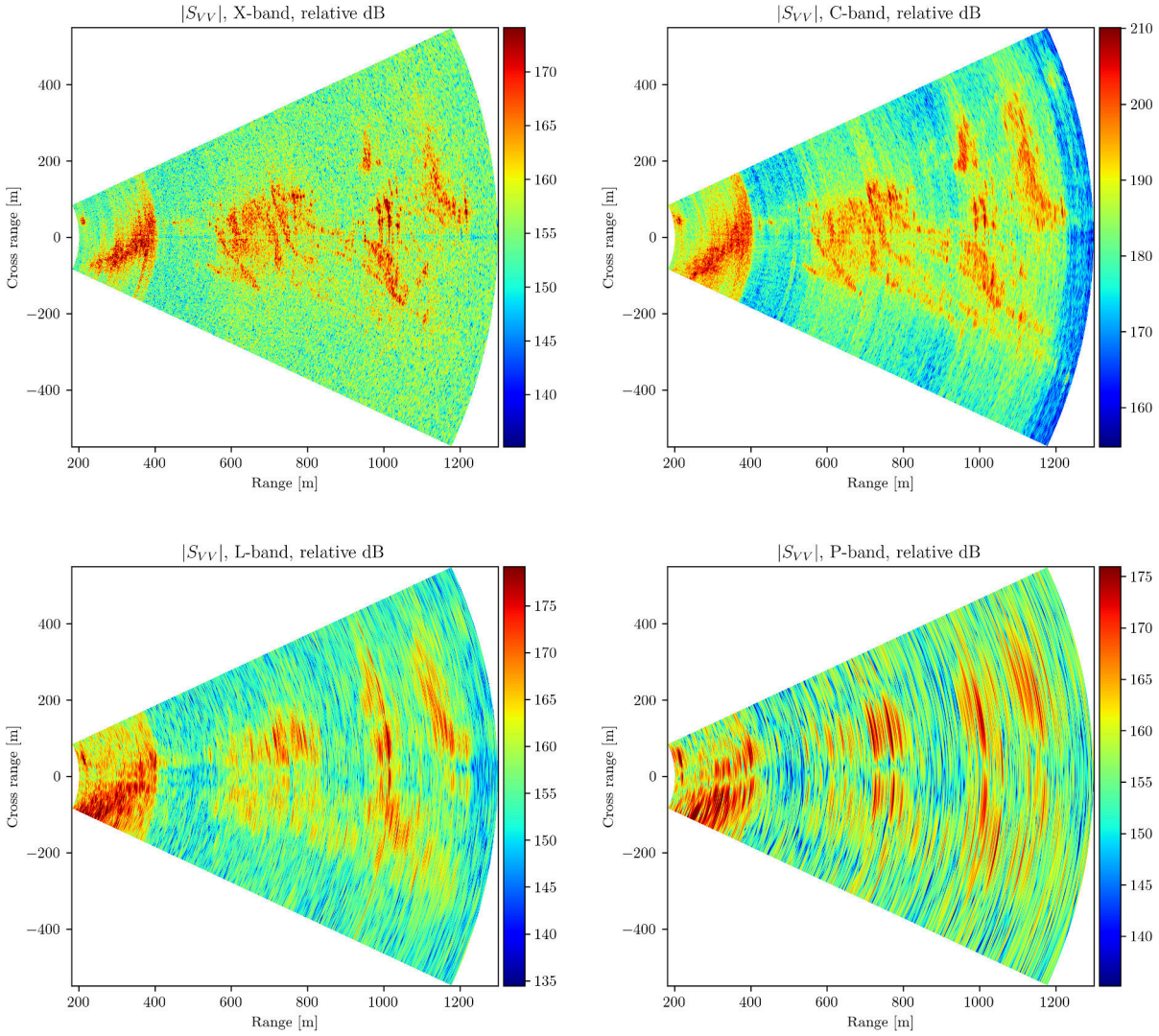

Figure 4.29: Magnitude images of the test site nº2. The absolute power is uncalibrated.

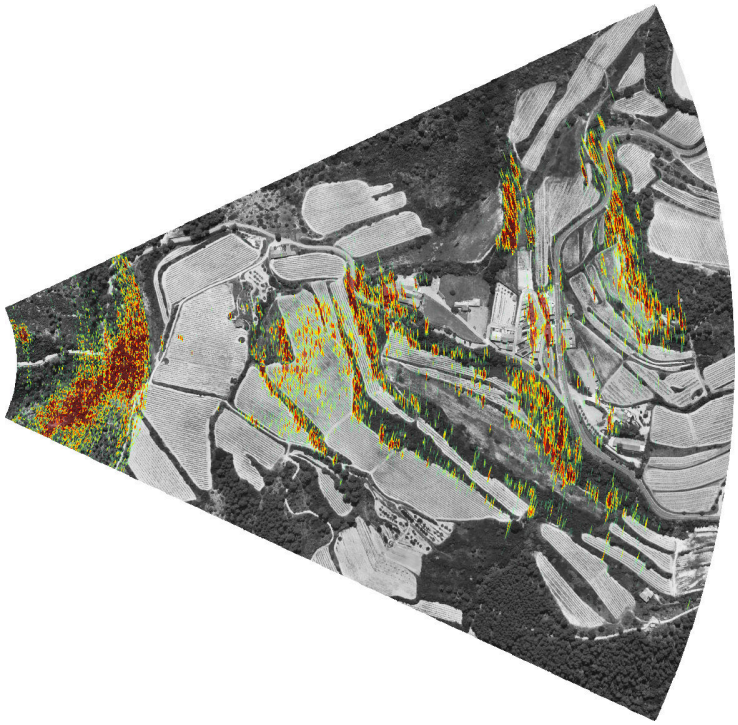

Figure 4.30: Composition of the orthophoto and the thresholded mangitude X-band GB-SAR image of the Subirats test site nº2. Orthophoto credit: ICGC.

in periodic broadband spurs that cannot be easily removed as done with the other spurs, that are concentrated only in the central part of sweep.

These chirp-like spurs are not easily seen with common signal analysis techniques such as the Discrete Fourier Transform (DFT) or the STFT due to the short-time signals involved. The Wigner-Ville distribution [89] proved to be a good tool to inspect these spurs, due to its superior time-frequency resolution characteristics. Figure 4.32 shows the Wigner-Ville transform of an averaged sweep, which shows the chirp-like spurs. This result helped in tracking the origin of the spurs, since its period and slope confirmed their origin.

The mechanism that explains the appearance of the spur only around zero azimuth is that the spurs are constant along slow-time, and overlap with the near constant return from zero-azimuth targets. A consequence of this mechanism is that the spur is thinner at higher bands, and broadens as the frequency gets lower.

A fix is taken into account in the next hardware revision. An interesting fact is that this spur was not detected in the early test campaigns, probably due to a better isolation between the reference clock and other parts of the system, as all devices were shielded individually. In the SLC images shown, a partial fix was applied by eliminating and extrapolating the DC component of the slow-time FFT. However, this is not an ideal fix as data is inevitably destroyed in the vicinity of zero azimuth. Nevertheless, further

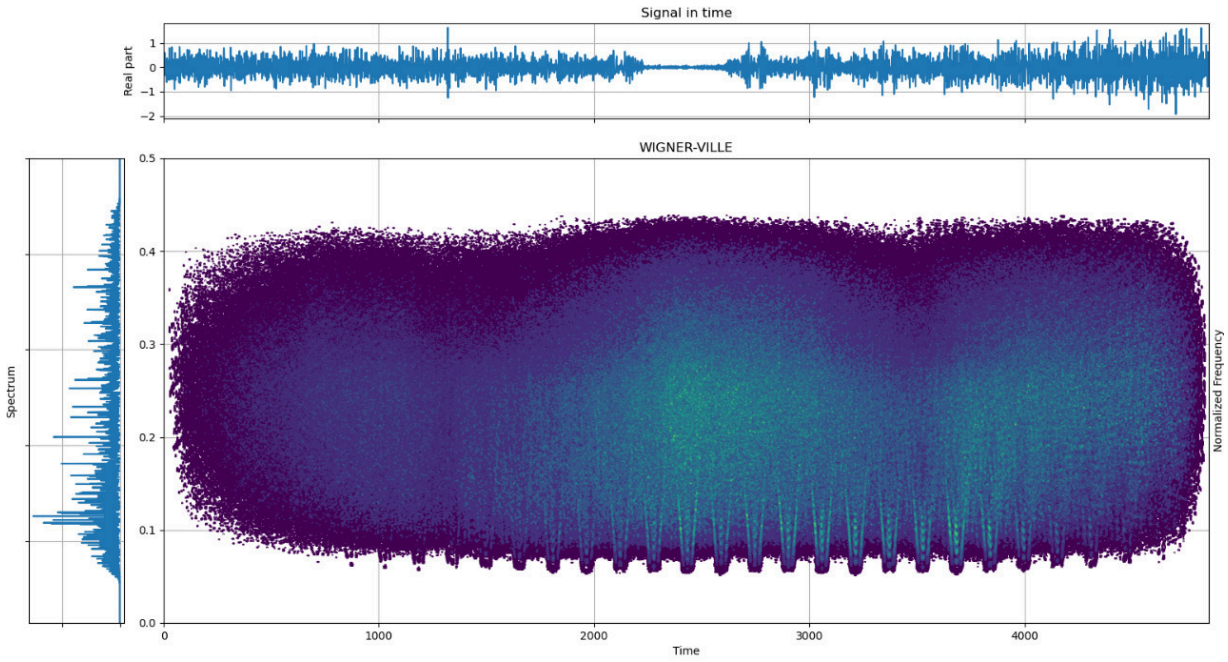

Figure 4.31: Wigner-Ville transform of the average of various sweeps.

processing can still be done with care.

The magnitude images in Figure 4.30 show that the strongest scatterers are the first layer of trees, man made structures, the slopes between the vineyard terraces, and various tree zones. The most notable difference can be seen in the first layer of trees, between a range of 200 m and 400 m. The azimuth extension of the high return area widens significantly from C- to L-band, indicating that the penetration depth increases. Another observation is the energy spread over azimuth, or blurring [90], of the vegetated areas. This effect is more evident at C-band, but is in theory stronger at X-band. However, at X-band, the background noise level is higher and the energy spread is buried under it. At L- and P-bands, this blurring effect is not evident due to a significant reduction of the wave interaction with vegetation leaves.

In this case, contrary to what is done at test site n^{o}1, coherence maps are computed. In these maps, the sampled coherence is computed within a sliding rectangular window. The window size is chosen so that the ENL is high enough to prevent excessive bias in low coherence areas, and kept as small as possible to limit the degradation of spatial resolution. Figure 4.34 shows the generated coherence maps for each frequency. The sliding window is chosen to lead approximately to an ENL value of 15. It is necessary to state that the polar SLC images are over-sampled in range and azimuth with a factor of 4 at X- and C-band, and with a factor of 40 at L- and P-bands, in order to yield smooth images. It is interesting to observe the general increase in coherence that happens

from X- to C-band. Being careful with the decrease in resolution, that can falsely give an impression of higher coherence, it is evident that C-band contains high coherence areas that exhibit very low coherence at X-band. This is the case, for example, of the tree area starting at 1000 m range. At L- and P-band, the reduced resolution makes this evaluation more difficult. However, there is a marked increase of high coherence pixels at the first layer of vegetation for P-band. In Figure 4.33 a more detailed view of this area is given. Comparing the magnitude images of Figure 4.30 and the coherence maps of Figure 4.34, the correlation between vegetation density and coherence in all bands can be clearly seen.

Figure 4.32: Detail of the first vegetated area from the Subirats castle test site nº1. Orthophoto credit: ICGC.

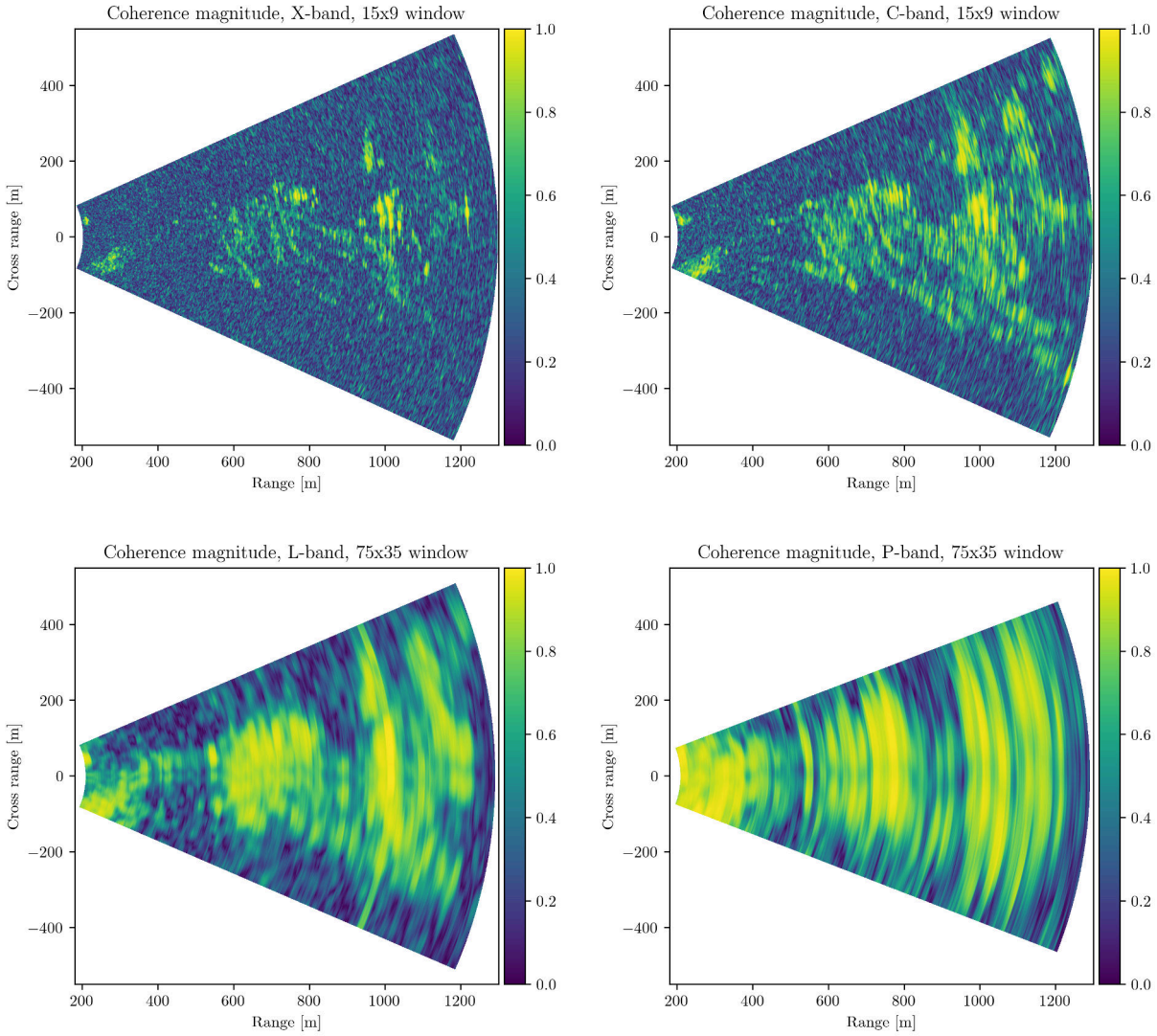

Figure 4.33: Coherence maps for all frequencies.

4.3.3 Test site nº 3

In order to image the third test site, the radar was repositioned to face North. The northern view from the Subirats castle is more diverse than in the second test site. A speedway, various roads, industrial buildings and a high speed train bridge combine with vineyards and other vegetated zones. The radar was located at 41°24'59.0"N 1°48'59.5"E, at an altitude of 285 m above sea level. As a reference, the height difference between the radar and the speedway is 146 m. An orthophoto and its corresponding elevation map are shown in Figure 4.35. The radar was configured to image an area between 200 m and 2 km. Only two images were taken at each band. The objectives of this test were the same as the one done at the second test site, but in this case the imaged area is more diverse. In Figure 4.36 the area from the radar point of view is shown, along with a detail of some vineyards and artificial structures. To assist in the comprehension of the geometry of the area, height and slope profiles are shown in Figure 4.37.

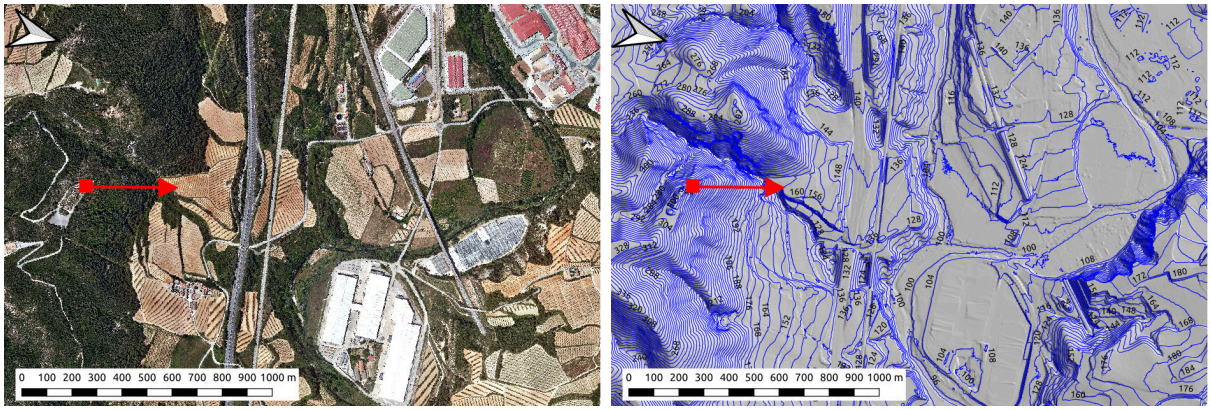

(a) (b)

Figure 4.34: Test site nº3 orthophoto and elevation map. The square and arrow indicate the radar position and azimuth view direction. Orthophoto and DEM credit: ICGC.

The magnitude images are shown in Figure 4.38, and the accompanying X-band thresholded magnitude composite image is shown in Figure 4.39 for reference. The zero-azimuth spur is still present in all images, being the L- and P-band images the most affected. Inspecting the X-band image, a good correlation can be done between the magnitude and the characteristics of the area. From low range to high range, the vineyards appears relatively strong (Figure 4.40a), followed by various smaller artificial reflectors such as metallic bridge railings (Figure 4.40b) or parked vehicles in a motorway rest area. Starting at 1 km, the strongest reflectors in the image can be seen, originating from the metallic shapes present in industrial buildings (Figure 4.40c). Advancing in range, other artificial buildings and structures such as bridges or electrical towers result in strong returns (Figure

(a)

(b)

(c)

Figure 4.35: (a) Test site nº3 from the radar point of view. (b) Vineyard area detail. (c) Detail of the area around the high speed train bridge.

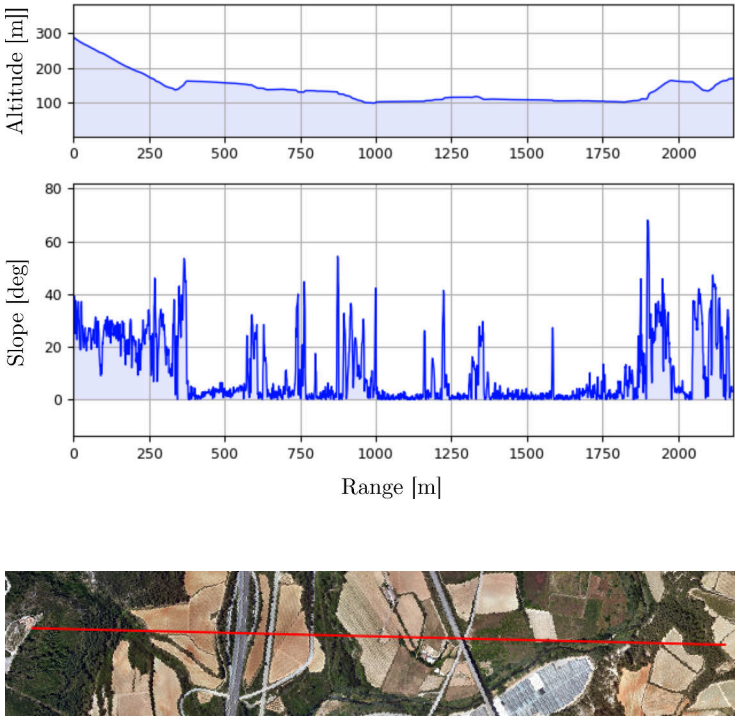

Figure 4.36: Height and slope profiles for the line path shown. The horizontal axis represents range. All dimensions are in meters. Orthophoto and DEM credit: ICGC.

4.40d), and the train bridge is also clearly seen.

At C-band the same effect observed in the second test area takes place, including the appearance of targets at higher azimuth angles due to the broadening of the antenna beam, and an increase in the dynamic range result of significantly less free-space loss. At L-band, the degradation in resolution and the central spur makes interpretation more difficult. An interesting observation is that the artificial structures around (1700,-100)m yield a much lower return relative to the rest of the image, indicating that the contributing reflectors are small compared with the L-band wavelength. At P-band the same observation can be done.

Regarding the coherence maps, that can be seen in Figure 4.41, the main observations are similar to the ones in test site nº2. From X- to C-band, a general increase in coherence takes place, and some areas that exhibit complete decorrelation at X-band, for example the area around (200, 1400)m become distinguishable at C-band. There are other highly coherent areas that appear due to the effect of the antenna beam broadening. At L- and P- bands the interpretation is more difficult. Nonetheless, it is clear that there is a coherence increase in the vineyards and the industrial buildings remain highly coherent. The dimming of the area at (1700,-100)m observed in the magnitude images is translated to the coherence map with a decrease in coherence magnitude due to a strong loss in SNR.

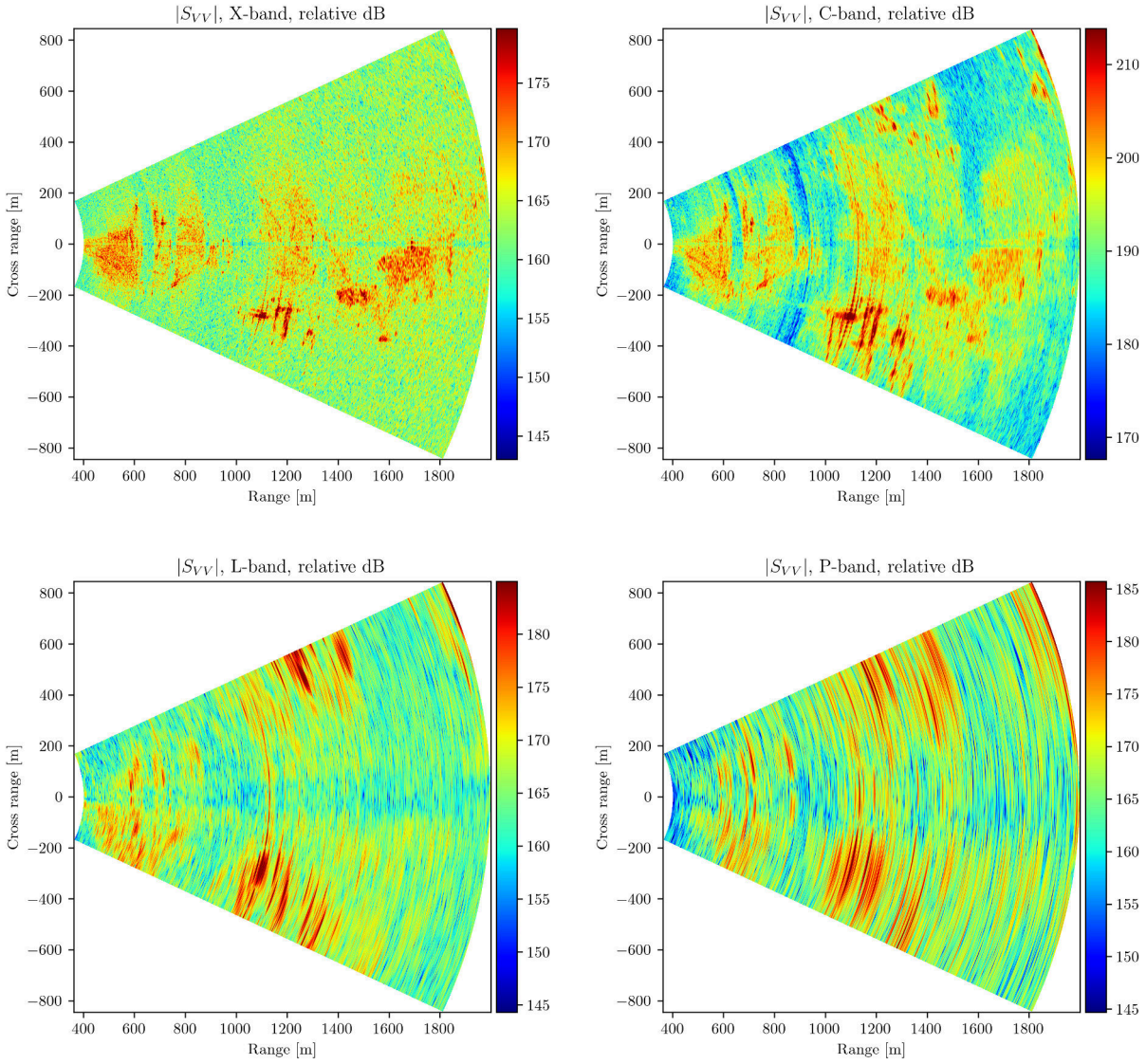

Figure 4.37: Magnitude images of the test site n°3. The absolute power is uncalibrated.

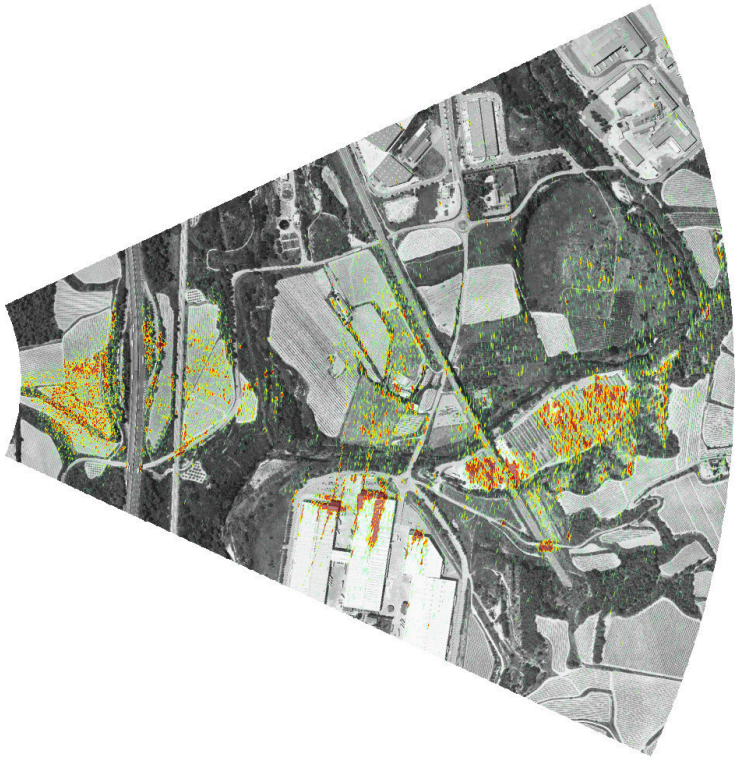

Figure 4.38: Composition of orthophoto and the thresholded magnitude X-band GBSAR image of the Subirats castle test site nº3. Orthophoto credit: ICGC.

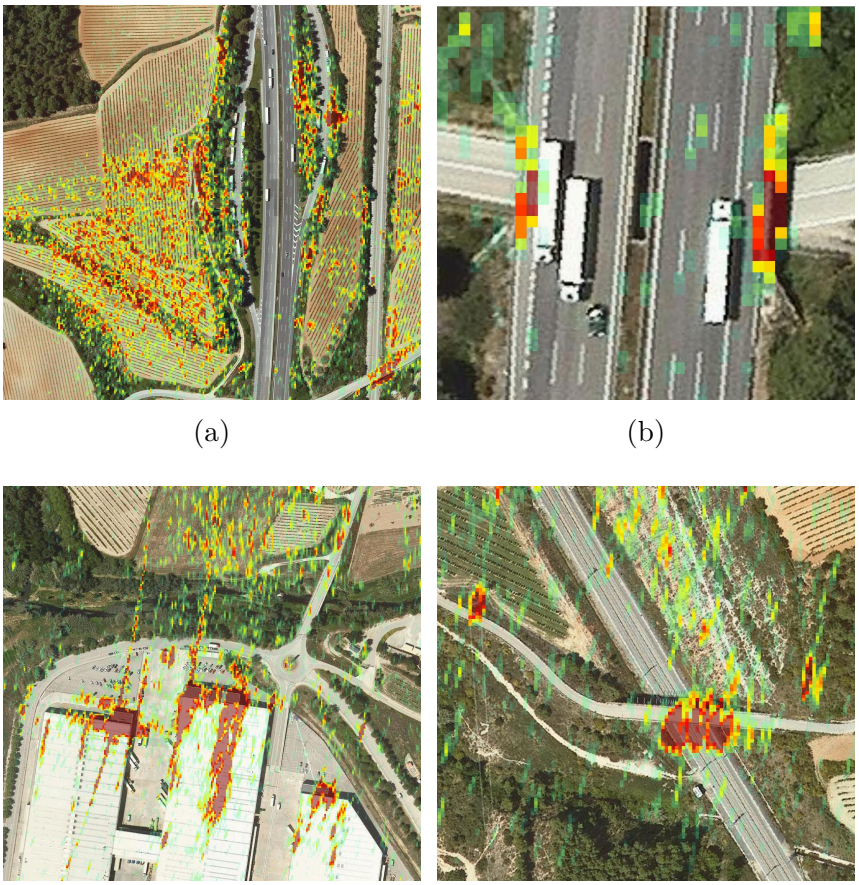

(a) (b)

(c) (d)

Figure 4.39: Details of the thresholded linear magnitude image for test site nº3.

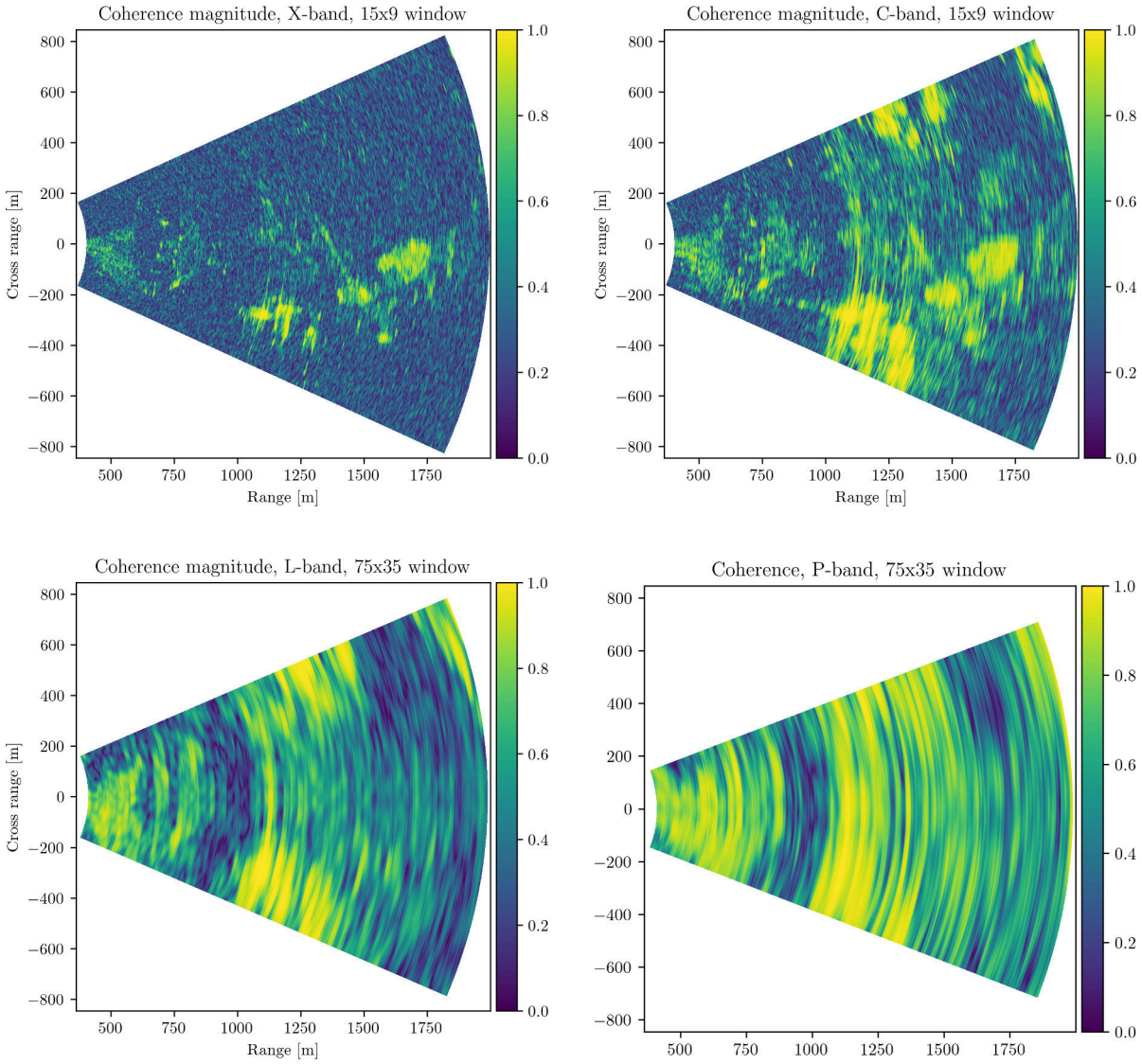

Figure 4.40: Coherence maps for all frequencies.

5 Conclusions and future work

This part is omitted due to non-disclosure agreements.

Bibliography

[1] K. El-Darymli, P. McGuire, D. Power, and C. Moloney, "Target detection in synthetic aperture radar imagery: a state-of-the-art survey," *Journal of Applied Remote Sensing*, vol. 7, no. 1, p. 071598, 2013.

[2] A. Anghel, G. Vasile, and R. Cacoveanu, *Infrastructure Monitoring with Spaceborne SAR Sensors*, ser. SpringerBriefs in Electrical and Computer Engineering. Springer Singapore, 2017.

[3] N. Joshi, M. Baumann, A. Ehammer, R. Fensholt, K. Grogan, P. Hostert, M. R. Jepsen, T. Kuemmerle, P. Meyfroidt, E. T. Mitchard, J. Reiche, C. M. Ryan, and B. Waske, "A review of the application of optical and radar remote sensing data fusion to land use mapping and monitoring," *Remote Sensing*, vol. 8, no. 1, pp. 1–23, 2016.

[4] A. Moreira, P. Prats-Iraola, M. Younis, G. Krieger, I. Hajnsek, and K. P. Papathanassiou, "A tutorial on synthetic aperture radar," *IEEE Geoscience and Remote Sensing Magazine*, vol. 1, no. 1, pp. 6–43, mar 2013.

[5] W. G. Carrara, R. M. Majewski, and R. S. Goodman, *Spotlight Synthetic Aperture Radar: Signal Processing Algorithms (Artech House Remote Sensing Library)*. Artech Print on Demand, 1995.

[6] M. I. Skolnik, *Radar Handbook*, 3rd ed. McGraw-Hill Education, 2008.

[7] J. B. Way and E. A. Smith, "The evolution of synthetic aperture radar systems and their progression to the EOS SAR," *IEEE Transactions on Geoscience and Remote Sensing*, vol. 29, no. 6, pp. 962–985, 1991.

[8] European Space Agency, "ERS-1 - eoPortal Directory - Satellite Missions." [Online]. Available: https://directory.eoportal.org/web/eoportal/satellite-missions/e/ers-1

[9] ——, "JERS-1 - eoPortal Directory - Satellite Missions." [Online]. Available: https://directory.eoportal.org/web/eoportal/satellite-missions/j/jers-1

[10] ——, "RADARSAT-1 -eoPortal Directory - Satellite Missions." [Online]. Available: https://directory.eoportal.org/web/eoportal/satellite-missions/r/radarsat-1

[11] J. Yang, Y. Yamaguchi, J. S. Lee, R. Touzi, and W. M. Boerner, "Applications of polarimetric SAR," *Journal of Sensors*, vol. 2015, pp. 11–13, 2015.

[12] D. Werner, "A New Hope for Commercial Space-based Radar," *Space News Magazine*, 2016.

[13] G. Filippazzo and S. Dinand, "The Potential Impact Of Small Satellite Radar Constellations On Traditional Space Systems," *Federated and Fractionated Satellite Systems Workshop*, vol. 5, pp. 1–12, 2017. [Online]. Available: http://golkar.scripts.mit.edu/fss/wp-content/uploads/2017/10/Paper-6.pdf

[14] "ESA Earth Online - ICEYE." [Online]. Available: https://earth.esa.int/web/guest/missions/3rd-party-missions/current-missions/iceye

[15] Copernicus Program, "Sentinel Satellite Family." [Online]. Available: https://www.copernicus.eu/en/about-copernicus/infrastructure/discover-our-satellites

[16] M. Lort Cuenca, "Contribution to ground-based and uav sar systems for the earth observation," Ph.D. dissertation, 2017.

[17] O. Monserrat, M. Crosetto, and G. Luzi, "A review of ground-based SAR interferometry for deformation measurement," *ISPRS Journal of Photogrammetry and Remote Sensing*, vol. 93, no. July, pp. 40–48, 2014. [Online]. Available: http://dx.doi.org/10.1016/j.isprsjprs.2014.04.001

[18] "SSR-SARx - GroundProbe." [Online]. Available: https://www.groundprobe.com/product/ssr-sarx/

[19] R. Iglesias, A. Aguasca, X. Fabregas, J. J. Mallorqui, D. Monells, C. Lopez-Martinez, and L. Pipia, "Ground-Based Polarimetric SAR Interferometry for the Monitoring of Terrain Displacement Phenomena. Part I: Theoretical Description," *Selected Topics in Applied Earth Observations and Remote Sensing, IEEE Journal of*, vol. 8, no. 3, pp. 980–993, 2015.

[20] I. Corporation, "IBIS-FM - IDS GeoRadar." [Online]. Available: https://idsgeoradar.com/products/interferometric-radar/ibis-fm

[21] "FastGBSAR-S | Geomatics." [Online]. Available: https://www.geomatics.metasensing.com/fastgbsar-s

[22] C. Hu, Y. Deng, W. Tian, J. Wang, and T. Zeng, "Novel MIMO-SAR system applied for high-speed and high-accuracy deformation measurement," *The Journal of Engineering*, vol. 2019, no. 20, pp. 6598–6602, oct 2019. [Online]. Available: https://digital-library.theiet.org/content/journals/10.1049/joe.2019.0290

[23] "PHOENIX | Echoes Radar Technologies." [Online]. Available: https://www.echoes-tech.it/portfolio/phoenix-gb-sar/

[24] "IRadar: A Smarter Way to Inspect, Analyze & Manage Data." [Online]. Available: https://www.iradarx.com/gbsar

[25] D. Tarchi, K. Lukin, D. Leva, J. Fortuni, A. Mogila, P. Vyplavin, and A. Sieber, "Implementation of Noise Radar Technology in Ground Based SAR for Short Range Applications," in *2007 International Kharkiv Symposium Physics and Engrg. of Millimeter and Sub-Millimeter Waves (MSMW)*. IEEE, jun 2007, pp. 442–444.

[26] D. Tarchi, "Monitoring landslide displacements by using ground-based synthetic aperture radar interferometry: Application to the Ruinon landslide in the Italian Alps," *Journal of Geophysical Research*, vol. 108, no. B8, 2003.

[27] S. C. Brown, S. Quegan, K. Morrison, J. C. Bennett, and G. Cookmartin, "High-resolution measurements of scattering in wheat canopies - Implications for crop parameter retrieval," *IEEE Transactions on Geoscience and Remote Sensing*, vol. 41, no. 7 PART I, pp. 1602–1610, 2003.

[28] H. Lee, J.-h. Lee, K.-e. Kim, N.-H. Sung, and S.-J. Cho, "Development of a Truck-Mounted Arc-Scanning Synthetic Aperture Radar," *IEEE Transactions on Geoscience and Remote Sensing*, vol. 52, no. 5, pp. 2773–2779, may 2014.

[29] Z. S. Zhou, W. M. Boerner, and M. Sato, "Development of a ground-based polarimetric broadband SAR system for noninvasive ground-truth validation in vegetation monitoring," *IEEE Transactions on Geoscience and Remote Sensing*, vol. 42, no. 9, pp. 1803–1810, 2004.

[30] W. Wiesbeck, "SDRS: software-defined radar sensors," in *IGARSS 2001. Scanning the Present and Resolving the Future. Proceedings. IEEE 2001 International Geoscience and Remote Sensing Symposium (Cat. No.01CH37217)*, vol. 7, no. C. IEEE, 2001, pp. 3259–3261.

[31] C. López-Martínez, L. Ferro-Famil, and A. Reigber, "Advances in multidimensional synthetic aperture radar signal processing," *Eurasip Journal on Advances in Signal Processing*, vol. 2010, 2010.

[32] M. Davidson, M. Chini, W. Dierking, S. Djavidnia, J. Haarpaintner, G. Hajduch, G. V. Laurin, M. Lavalle, C. López-Martínez, T. Nagler, N. Pierdicca, and B. Su, "Copernicus L-band SAR Mission Requirements Document, Revision 2.0," 2019. [Online]. Available: https://esamultimedia.esa.int/docs/EarthObservation/CopernicusL-band_SAR_mission_ROSE-L_MRD_v2.0_issued.pdf

[33] J. Mitola, "Software radios-survey, critical evaluation and future directions," in *[Proceedings] NTC-92: National Telesystems Conference*, 1992, pp. 13/15–13/23.

[34] M. Dillinger, K. Madani, N. Alonistioti, M. Dillinger, K. Madani, and N. Alonistioti, "Software Defined Radio: Architectures, Systems, and Functions," 2003.

[35] A. M. Wyglinski, R. Getz, T. Collins, and D. Pu, *Software-Defined Radio for Engineers*, ser. Artech House mobile communications series. Artech House, 2018. [Online]. Available: https://books.google.es/books?id=cKR5DwAAQBAJ

[36] IEEE, "IEEE Standard for Definitions and Concepts for Dynamic Spectrum Access: Terminology Relating to Emerging Wireless Networks, System Functionality, and Spectrum Management," 2019. [Online]. Available: https://standards.ieee.org/develop/project/1900.1.html

[37] "About USRP Bandwidths and Sampling Rates. AN-177 - Ettus Knowledge Base." [Online]. Available: https://kb.ettus.com/About_USRP_Bandwidths_and_Sampling_Rates

[38] "Intel® Agilex™ FPGAs and SoCs FPGA Family." [Online]. Available: https://www.intel.com/content/www/us/en/products/programmable/fpga/agilex.html

[39] "Zynq-7000 SoC." [Online]. Available: https://www.xilinx.com/products/silicon-devices/soc/zynq-7000.html

[40] "Numba: A High Performance Python Compiler." [Online]. Available: http://numba.pydata.org/

[41] NVIDIA Corporation, "GPUDirect - NVIDIA Developer," 2020-04-07. [Online]. Available: https://developer.nvidia.com/gpudirect

[42] E. Grayver, *Implementing Software Defined Radio*. New York, NY: Springer New York, 2013. [Online]. Available: http://link.springer.com/10.1007/978-1-4419-9332-8

[43] J. Reed, *Software Radio: A Modern Approach to Radio Engineering*, 1st ed. USA: Prentice Hall Press, 2002.

[44] B. Brannon, "Where Zero-IF Wins : 50 % Smaller PCB Footprint at 1 / 3 the Cost," *AnalogDialogue*, no. September, pp. 1–7, 2016.

[45] B. Razavi, *RF Microelectronics*, ser. Communications Engineering & Emerging Technology Series from Ted Rappaport. Pearson Education, 2011.

[46] D. Terlep, "Mixer 2x2 Spurious Response and IP2 Relationship," 2002.

[47] A. Michelini, F. Viviani, and L. Mayer, "Introduction to IBIS-ArcSAR: a circular scanning GB-SAR system for deformation monitoring," *4th Joint International Symposium on Deformation Monitoring (JISDM)*, no. May, pp. 15–17, 2019. [Online]. Available: https://jisdm2019.org/wp-content/uploads/2019/05/72.pdf

[48] M. Pieraccini and L. Miccinesi, "ArcSAR: Theory, Simulations, and Experimental Verification," *IEEE Transactions on Microwave Theory and Techniques*, vol. 65, no. 1, pp. 293–301, jan 2017.

[49] D. Tarchi, F. Oliveri, and P. F. Sammartino, "MIMO radar and ground-based SAR imaging systems: Equivalent approaches for remote sensing," *IEEE Transactions on Geoscience and Remote Sensing*, vol. 51, no. 1, pp. 425–435, 2013.

[50] J. Broussolle, V. Kyovtorov, M. Basso, G. Ferraro Di Silvi E Castiglione, J. Figueiredo Morgado, R. Giuliani, F. Oliveri, P. F. Sammartino, and D. Tarchi, "MELISSA, a new class of ground based InSAR system. An example of application in support to the Costa Concordia emergency," *ISPRS Journal of Photogrammetry and Remote Sensing*, vol. 91, pp. 50–58, 2014. [Online]. Available: http://dx.doi.org/10.1016/j.isprsjprs.2014.02.003

[51] G. Krieger, "MIMO-SAR: Opportunities and pitfalls," *IEEE Transactions on Geoscience and Remote Sensing*, vol. 52, no. 5, pp. 2628–2645, 2014.

[52] A. Michelini, F. Coppi, A. Bicci, and G. Alli, "SPARX, a MIMO array for ground-based radar interferometry," *Sensors (Switzerland)*, vol. 19, no. 2, jan 2019.

[53] M. Soumekh, *Synthetic Aperture Radar Signal Processing with MATLAB Algorithms*. Wiley, 1999.

[54] R. J. Sullivan, *Radar Foundations for Imaging and Advanced Concepts*. SciTech Publishing, 2004.

[55] L. Pipia, "Polarimetric differential SAR Interferometry with ground-based sensors," Ph.D. dissertation, 2009.

[56] L. K. Patton, "A GNU Radio Based Software-Defined Radar," 2007.

[57] "Synchronizing USRP Events Using Timed Commands in UHD. AN-883 - Ettus Knowledge Base." [Online]. Available: https://kb.ettus.com/Synchronizing_USRP_Events_Using_Timed_Commands_in_UHD

[58] G. Aloi, G. D. Massa, P. Pace, S. Constanzo, G. Di Massa, F. Spadafora, E. Natalizio, and V. Loscri, "Software Defined Radar : synchronization issues and practical implementation," *4th International Conference on Cognitive Radio and Advanced Spectrum Management*, pp. 48–52, 2011.

[59] M. T. Frankford, N. Majurec, and J. T. Johnson, "Software-defined radar for MIMO and adaptive waveform applications," *IEEE National Radar Conference - Proceedings*, pp. 724–728, 2010.

[60] T. C. Mealey and A. J. Duly, "BEEMER: A firmware-tuned, software-defined MIMO radar testbed," in *IEEE International Symposium on Phased Array Systems and Technology*, 2016.

[61] M. Braun, J. Pendlum, and M. Ettus, "RFNoC: RF Network-on-Chip," *Proceedings of the GNU Radio Conference*, vol. 1, no. 1, 2016. [Online]. Available: https://pubs.gnuradio.org/index.php/grcon/article/view/3

[62] D. Petri, F. Berizzi, M. Martorella, E. Dalle Mese, and A. Capria, "A software defined UMTS passive radar demonstrator," in *4th Microwave and Radar Week MRW-2010 - 11th International Radar Symposium, IRS 2010 - Conference Proceedings*, 2010, pp. 44–47.

[63] C. W. Rossler, E. Ertin, and R. L. Moses, "A software defined radar system for joint communication and sensing," in *IEEE National Radar Conference - Proceedings*, 2011, pp. 1050–1055.

[64] T. Nagarmat, "Interferometric Techniques in Software Defined Radars," Ph.D. dissertation, 2012.

[65] S. M. Bostan, J. V. Urbina, J. D. Mathews, S. G. Bilén, and J. K. Breakall, "An HF Software-Defined Radar to Study the Ionosphere," *Radio Science*, vol. 54, no. 9, pp. 839–849, 2019.

[66] P. Liu, J. Mendoza, H. Hu, P. G. Burkett, J. V. Urbina, S. Anandakrishnan, and S. G. Bilén, "Software-Defined Radar Systems for Polar Ice-Sheet Research," *IEEE JOURNAL OF SELECTED TOPICS IN APPLIED EARTH OBSERVATIONS AND REMOTE SENSING*, vol. 12, no. 3, p. 803, 2019.

[67] S. Costanzo, F. Spadafora, A. Borgia, O. Moreno, A. Costanzo, G. Di Massa, H. O. Moreno, A. Costanzo, and G. Di Massa, "High resolution software defined radar system for target detection," *Advances in Intelligent Systems and Computing*, vol. 206 AISC, 2013.

[68] F. Spadafora, G. D. Massa, A. Borgia, A. Costanzo, G. Aloi, P. Pace, and V. Loscr, "Potentialities of Usrp-Based Software Defined Radar Systems," *Progress In Electromagnetics Research B*, vol. 53, no. August, pp. 417–435, 2013.

[69] S. Costanzo, G. Di Massa, A. Costanzo, A. Borgia, A. Raffo, G. Viggiani, and P. Versace, "Software-defined radar system for landslides monitoring," in *Advances in Intelligent Systems and Computing*, vol. 445, 2016, pp. 325–331.

[70] Y.-K. Kwag, J.-S. Jung, I.-S. Woo, and M.-S. Park, "Modern Software Defined Radar (SDR) Technology and Its Trends," *Journal of electromagnetic engineering and science*, vol. 14, no. 4, pp. 321–328, dec 2014. [Online]. Available: http://koreascience.or.kr/journal/view.jsp?kj=E1ELAT{&}py=2014{&}vnc=v14n4{&}sp=321

[71] Y.-K. Kwag, I.-S. Woo, H.-Y. Kwak, and Y.-H. Jung, "Multi-mode SDR radar platform for small air-vehicle Drone detection," in *2016 CIE International Conference on Radar (RADAR)*, vol. 9. IEEE, oct 2016, pp. 1–4.

[72] J. Pancik and M. Pancik, "Hardware and software front-end based on the USRP for experimental X-band Synthetic Aperture Radar," *Proceedings of 25th International Conference Radioelektronika, RADIOELEKTRONIKA 2015*, pp. 154–159, 2015.

[73] A. Grabowski, "SDR-based LFM signal generator for radar/SAR systems," in *2016 17th International Radar Symposium (IRS)*, vol. 0, no. 2. IEEE, may 2016, pp. 1–3.

[74] J. Marimuthu, K. S. Bialkowski, and A. M. Abbosh, "Software-defined radar for medical imaging," *IEEE Transactions on Microwave Theory and Techniques*, vol. 64, no. 2, pp. 643–652, 2016.

[75] J. Hershberger, T. Pratt, and R. Kossler, "A software-defined, dual-polarized radar system," in *2016 IEEE Conference on Antenna Measurements & Applications (CAMA)*, no. 1. IEEE, oct 2016, pp. 1–4.

[76] ——, "Implementations of Coherent Software-Defined Dual-Polarized Radars," *IEEE Transactions on Microwave Theory and Techniques*, vol. 65, no. 5, pp. 1673–1681, 2017.

[77] B. Kirk, J. Owen, K. Gallagher, A. Martone, K. Sherbondy, R. Narayanan, and S. Blunt, "Development of a Software-Defined Radar," 2017.

[78] B. H. Kirk, J. W. Owen, R. M. Narayanan, S. D. Blunt, A. F. Martone, and K. D. Sherbondy, "Cognitive software defined radar: waveform design for clutter and interference suppression," *Radar Sensor Technology XXI*, vol. 10188, p. 1018818, 2017.

[79] S. C. Carey, "Software defined radio for stepped-frequency, ground-penetrating radar," no. May, p. 70, 2017.

[80] S. Prager, T. Thrivikraman, M. Haynes, J. Stang, D. Hawkins, and M. Moghaddam, "Ultra-wideband synthesis for high-range resolution software defined radar," *2018 IEEE Radar Conference, RadarConf 2018*, no. ii, pp. 1089–1094, 2018.

[81] M. Vidal-Morera, "Simulation of FMCW Radar Systems Based on Software Defined Radio," in *Proceedings of the 6th GNU Radio Conference*, 2016.

[82] L. Noferini, M. Pieraccini, D. Mecatti, G. Luzi, C. Atzeni, A. Tamburini, and M. Broccolato, "Permanent scatterers analysis for atmospheric correction in ground-based SAR interferometry," *IEEE Transactions on Geoscience and Remote Sensing*, vol. 43, no. 7, pp. 1459–1470, 2005.

[83] A. Ferretti, C. Prati, and F. Rocca, "Permanent scatterers in SAR interferometry," *IEEE Transactions on Geoscience and Remote Sensing*, vol. 39, no. 1, pp. 8–20, 2001.

[84] R. Touzi, A. Lopes, J. Bruniquel, and P. W. Vachon, "Coherence estimation for SAR imagery," *IEEE Transactions on Geoscience and Remote Sensing*, vol. 37, no. 1 PART 1, pp. 135–149, 1999.

[85] K. P. Papathanassiou, A. Reigber, and M. Coltelli, "On the interferometric coherence: A multifrequency and multitemporal analysis," *European Space Agency, (Special Publication) ESA SP*, vol. (5)2, no. 406, pp. 319–329, 1997.

[86] M. Crosetto, O. Monserrat, G. Luzi, N. Devanthéry, M. Cuevas-González, and A. Barra, "Data Processing and Analysis Tools Based on Ground-Based Synthetic Aperture Radar Imagery," *ISPRS - International Archives of the Photogrammetry, Remote Sensing and Spatial Information Sciences*, vol. XLII-2/W7, pp. 593–596, sep 2017. [Online]. Available: https://www.int-arch-photogramm-remote-sens-spatial-inf-sci.net/XLII-2-W7/593/2017/

[87] "Generalized Hypergeometric Function | Wolfram MathWorld." [Online]. Available: https://mathworld.wolfram.com/GeneralizedHypergeometricFunction.html

[88] C. Oliver and S. Quegan, *Understanding synthetic aperture radar images(Book)*, 1997.

[89] L. Debnath, *The Wigner-Ville Distribution and Time-Frequency Signal Analysis*. Boston, MA: Birkhäuser Boston, 2002, pp. 307–360. [Online]. Available: https://doi.org/10.1007/978-1-4612-0097-0_5

[90] M. Lort, A. Aguasca, C. Lopez-Martinez, and X. Fabregas, "Impact of Wind-Induced Scatterers Motion on Gb-SAR Imaging," *IEEE Journal of Selected Topics in Applied Earth Observations and Remote Sensing*, vol. 11, no. 10, pp. 3757–3768, 2018.

Appendices

This part is omitted due to non-disclosure agreements.